

Spectral-Domain-Based Scattering Analysis of Fields Radiated by Distributed Sources in Planar-Stratified Environments with Arbitrarily Anisotropic Layers

Kamalesh Sainath^{1,*} and Fernando L. Teixeira^{1,†}

¹*The Ohio State University: ElectroScience Laboratory[‡]*

(Dated: March 31, 2014)

Abstract

We discuss the numerically stable computation and extraction of the scattered electromagnetic field excited by distributed sources embedded in planar-layered environments where each layer may exhibit arbitrary and independent electrical and magnetic anisotropic response and loss profiles. Although the scattered field computation appears analytically relatively straightforward, different procedures within the computation chain, if not treated carefully, are inherently susceptible to numerical instabilities and (or) accuracy limitations due to the potential manifestation of numerically overflowed and (or) numerically unbalanced terms entering the chain. Therefore, primary emphasis is given to effecting these tasks in a numerically stable and robust manner for all ranges of physical parameters. We validate the results against closed-form solutions and provide a computational efficiency study demonstrating a drastic reduction in computation time realized via the spectral domain (i.e., k -space or, equivalently, momentum space) decomposition of the distributed source field excitation. Finally, we illustrate the applicability of the proposed algorithm in a case study concerning active remote sensing of marine hydrocarbon reserves embedded deep within lossy, planar-layered media.

PACS numbers: 02.70.-c, 02.70.Hm, 95.75.Pq

Keywords: Sommerfeld integral; anisotropic media; integral acceleration; Green's function; stratified media

* sainath.1@osu.edu

† teixeira@ece.osu.edu

‡ Address: 1330 Kinnear Road, Columbus, Ohio, USA 43212

I. INTRODUCTION

Computation of electromagnetic (EM) fields radiated by current distributions, embedded within planar-stratified environments with generally anisotropic media characterized by arbitrary (diagonalizable) 3×3 relative permeability and permittivity tensors $\bar{\boldsymbol{\mu}}_r$ and $\bar{\boldsymbol{\epsilon}}_r$, finds application in myriad areas. Some examples are geophysical prospection in subterranean media using induction tools and borehole radars [1–13], analysis of microstrip antennas radiating over engineered substrates [14–17], planar waveguide analysis [18], transionospheric EM propagation studies [19], near-subsurface prospection using ground penetrating radar (GPR) [20], active remote sensing of deeply buried marine hydrocarbon formations using controlled source electromagnetic (CSEM) tools [21–31], and so on. To facilitate field computation in such problems that typically exhibit electrically large domains, pseudo-analytical methods comprising of rigorously phrasing the space-domain EM field solution in terms of either one-dimensional or two-dimensional spectral (Fourier-type) integral representations represent a robust class of fast numerical evaluation techniques [32–37]. For example, as demonstrated in [34], through use of Complex-Plane Gauss-Laguerre Quadrature (CGLQ) and adaptive *hp* refinement one can rapidly and accurately evaluate, without analytical-stage¹ approximations, the radiated EM field via direct numerical integration without major concern about slow integrand decay (and hence slow convergence) or rapid integrand oscillation (necessitating fine sampling and high computational cost).

As usual, the (scattered) space-domain electric field $\boldsymbol{\mathcal{E}}_s(\mathbf{r})$ is written here as the perturbation on the field due to presence of the environment inhomogeneity, that is $\boldsymbol{\mathcal{E}}_s(\mathbf{r}) = \boldsymbol{\mathcal{E}}(\mathbf{r}) - \delta_{L,M}\boldsymbol{\mathcal{E}}_d(\mathbf{r})$, where $\boldsymbol{\mathcal{E}}(\mathbf{r})$ is the total field, $\boldsymbol{\mathcal{E}}_d(\mathbf{r})$ is the “direct” field in the absence of any inhomogeneity, and the Kronecker delta symbol $\delta_{L,M}$ equals either one or zero when the source and observation layers (M and L , resp.) either coincide or differ, respectively. In most of the application areas above, the scattered field constitutes the signal of interest as it carries information about the medium under interrogation. For example, in geophysical borehole prospection it is well known that planar inhomogeneity can lead to erroneous extraction of the resistivity tensor of the local earth formation in which the sonde is presently embedded; one such phenomenon is known as the “shoulder bed” effect [11]. Therefore, being able to extract and analyze only the scattered field contribution may facilitate mitigating

¹ As opposed to e.g., image and asymptotic methods [38][Ch. 2][39, 40].

formation inhomogeneity effects in sonde measurements and thereby potentially increase the accuracy of the inverted formation’s resistivity profile along the borehole. Similarly concerning radars, one is usually only interested in the scattered field as it carries information about the parameter(s) of interest [20, 41–46] such as, for example, layer depth profiles [20] and soil moisture content [41, 46]. Two straightforward ways to effect scattered field extraction are (1) *a-posteriori* subtraction of the “direct” field response from the (numerically evaluated) total observed field composed of the scattered and direct field contributions and (2) time-gating, consisting of temporal windowing of the time domain (TD) direct and scattered field signals. There are important drawbacks with each of these two methods, however. The subtraction method suffers from lack of general applicability when the source is embedded in generally anisotropic media wherein the space domain tensor Green’s functions may not be available in closed form, as well as (even when the latter are available) (2) lack of robustness in the numerical evaluation since total and direct field component magnitudes can both become extremely large in the limit as the source and observation points coincide (e.g., when simulating the received time-harmonic scattered EM field presented to a mono-static radar), leading to the subtraction of two numerically overflowed results. Time-gating, on the other hand, is typically applicable only when the direct and scattered field contributions are well separated in time, which is often not the case in practice or when computing *time-harmonic* fields that inherently lack, in their time history, resolution between the direct and scattered fields. In contrast, the extraction approach proposed relies upon “in-situ” subtraction of the direct field during the modal field synthesis (i.e., spectral integration) process itself. This approach sports the following advantages:

1. Applicability to time-harmonic fields.
2. Does not depend upon the availability of analytical expressions for the space-domain tensor Green’s functions.
3. Robustness and numerical stability even as the source point $\mathbf{r}' = (x', y', z')$ approaches or equals the observation point $\mathbf{r} = (x, y, z)$.
4. Imposes no additional computational burden versus computing the total field [32–34].
5. Imparts added exponential decay to the spectral integrand that, when combined the

integration path deformation-based method discussed in [34], further accelerates convergence of the field solution.

6. Rigorously effects the time-windowing function ordinarily performed after synthesis of the TD total field signal.
7. Applicability to arbitrary antenna geometries whose radiated field is amenable to characteristic mode synthesis via a spectral integral, such as the two-dimensional Fourier integral, one-dimensional Fourier-Hankel integral, and one-dimensional Sommerfeld (i.e., Fourier-Bessel [47]) integral.

A robust and computationally accurate scattered-field extraction method, which generalizes a previously proposed extraction method for scalar fields due to point sources in isotropic, planar-layered media [48] to the more general case of vector fields in generally anisotropic layers, embodies the first major contribution of this work.

Besides extracting the scattered field, we also propose a novel algorithm to compute the spectral domain (i.e., k -space or, equivalently, momentum space) integral representation of the field produced by distributed sources embedded in such media. This strategy is based on the spectral decomposition of compactly-supported, otherwise arbitrary distributed sources in terms of a Fourier series and is useful in applications where realistic modeling of antennas is otherwise prohibitive due to the computationally expensive task of repeatedly computing the (space-domain) tensor Green's function followed by radiation integral evaluation. One such example includes computing the field at a spaceborne mono-static or bi-static radar receiver where the scattered field may have interacted with an inhomogeneous atmospheric and (or) subsurface environment [49, 50]. This approach is also desirable in aperture synthesis, where it can separately compute the field pattern of (orthogonal) Fourier modes radiating in a given inhomogeneous, anisotropic environment, and thus constitute an efficient forward engine for optimization algorithms in aperture field synthesis (inverse problem) to yield a desired far-zone field pattern².

We discuss the above-mentioned stability and robustness issues, along with the proposed solutions to them, in Sections III and IV. First for convenience, we briefly summarize notation conventions used herein and (in the next section) some fundamentals behind the

² We emphasize, however, that the proposed spectral-domain algorithm is not just applicable to finding far-zone fields, but rather the fields in *any* region (i.e., far-zone, intermediate-zone, and near-zone fields [51]).

underlying formulation. More details can be found in [32], with further numerical optimizations discussed in [33, 34]. Our notation usage is summarized as follows:

1. Boldface script denotes tensor, matrix, and vector quantities; the former two types also have an over-bar. Example for a tensor and a vector (resp.): $\bar{\mathbf{G}}$ and \mathbf{r} .
2. Unit-normalized vectors have an over-hat symbol. Example: $\hat{\mathbf{x}}$.
3. Spectral-domain quantities (besides the wave vector \mathbf{k}) have an over-tilde. Example: A modal electric field vector $\tilde{\mathbf{e}}$.
4. Space-domain quantities are demarcated with calligraphic script. Example: Space-domain electric field \mathcal{E} .
5. Mode-specific (mode-independent) quantities appear in lower (upper) case, respectively. Example: $\tilde{\mathbf{e}}_{L,n}$ is the n th modal electric field supported in layer L , while $\tilde{\mathbf{E}}$ is the mode-independent, spectral-domain electric field vector.

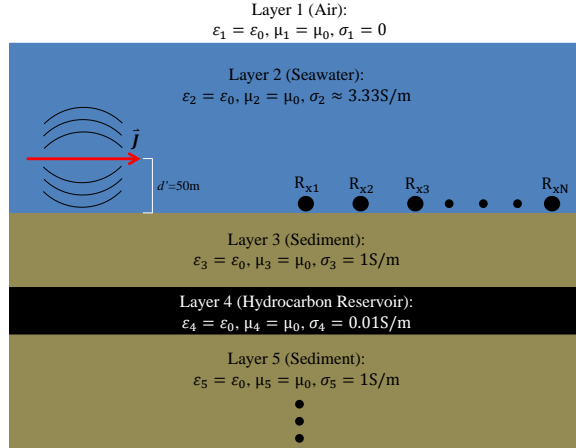


FIG. 1: Schematic illustration of a typical geophysical model employed in forward modeling studies concerning the CSEM method [28, 30]. A high-power wire antenna (represented by the red arrow and symbol $\vec{\mathcal{J}}$) transmits a waveform received by an array of N recording instruments located at the seafloor (symbolized by black circles, with the n th receiver labeled R_{xn}) [29].

II. FORMULATION FUNDAMENTALS: OVERVIEW

Initially assume a homogeneous medium possessing material tensors³ $\bar{\epsilon}_c = \epsilon_0 \bar{\epsilon}_r$ (generalized permittivity⁴) and $\bar{\mu}_c = \mu_0 \bar{\mu}_r$ (generalized permeability) exhibiting arbitrary and independent anisotropy and loss, in which there are impressed (i.e., causative) electric and (equivalent) magnetic current densities $\mathcal{J}(\mathbf{r})$ and $\mathcal{M}(\mathbf{r})$ (resp.), as well as impressed volumetric electric and (equivalent) magnetic charge densities ρ_v and ρ_m (resp.). From Maxwell's equation, one obtains [32, 38]:

$$\bar{\mathcal{A}} = \nabla \times \bar{\mu}_r^{-1} \cdot \nabla \times -k_0^2 \bar{\epsilon}_r. \quad (\text{II.1})$$

$$\bar{\mathcal{A}} \cdot \mathcal{E} = ik_0 \eta_0 \mathcal{J} - \nabla \times \bar{\mu}_r^{-1} \cdot \mathcal{M} \quad (\text{II.2})$$

where the $\exp(-i\omega t)$ convention is assumed and suppressed. Subsequently, defining the three-dimensional Fourier Transform (FT) pair, for some generic vector field \mathcal{L} [32]

$$\tilde{\mathbf{L}}(\mathbf{k}) = \iiint_{-\infty}^{+\infty} \mathcal{L}(\mathbf{r}) e^{-i\mathbf{k} \cdot \mathbf{r}} dx dy dz \quad (\text{II.3})$$

$$\mathcal{L}(\mathbf{r}) = \left(\frac{1}{2\pi}\right)^3 \iiint_{-\infty}^{+\infty} \tilde{\mathbf{L}}(\mathbf{k}) e^{i\mathbf{k} \cdot \mathbf{r}} dk_x dk_y dk_z \quad (\text{II.4})$$

with $\mathbf{r} = (x, y, z)$ and $\mathbf{k} = (k_x, k_y, k_z)$, one can take the FT of (II.2) to yield its Fourier domain version followed by multiplying $\tilde{\bar{\mathbf{A}}}^{-1}$ on both sides of the resultant Fourier-domain expression. Next, taking the triple inverse Fourier integral on both sides and analytically performing the k_z contour integration yields the formulation for the space domain field radiated by the source distribution. The very same steps above can be taken in a layered medium with $P = 1, \dots, N$ layers, with source in layer M and observation point in layer L (these layers may coincide). In this case, the integration over k_z yields $\mathcal{E}(\mathbf{r}) = \delta_{L,M} \mathcal{E}_d(\mathbf{r}) + \mathcal{E}_s(\mathbf{r})$ where both $\mathcal{E}_d(\mathbf{r})$ and $\mathcal{E}_s(\mathbf{r})$ are defined in terms of two-dimensional spectral integrals over the spectral (k_x, k_y) plane and $\delta_{L,M}$ is the Kronecker delta. Assuming a single Hertzian dipole source at \mathbf{r}' and denoting the observation point as \mathbf{r} , one has the expression for $\mathcal{E}_d(\mathbf{r})$,

³ ϵ_0 , c , and $\mu_0 = 1/(\epsilon_0 c^2)$ are the vacuum permittivity, speed of light, and permeability, resp. Similarly,

$\omega = 2\pi f$, $k_0 = \omega/c$, and $\eta_0 = \sqrt{\mu_0/\epsilon_0}$ are the angular radiation frequency, vacuum wavenumber and intrinsic impedance [38, 51], respectively, while i denotes the unit imaginary number.

⁴ That is, this tensor includes any polarization and conduction losses.

which is the “direct” field in the absence of planar inhomogeneity [32]:

$$\mathcal{E}_d(\mathbf{r}) = \frac{i}{(2\pi)^2} \iint_{-\infty}^{+\infty} \left[u(z - z') \sum_{n=1}^2 \tilde{a}_{M,n} \tilde{\mathbf{e}}_{M,n} e^{i\tilde{k}_{M,n}z} + u(z' - z) \sum_{n=3}^4 \tilde{a}_{M,n} \tilde{\mathbf{e}}_{M,n} e^{i\tilde{k}_{M,n}z} \right] \times e^{ik_x \Delta x + ik_y \Delta y} dk_x dk_y \quad (\text{II.5})$$

where $\Delta z = z - z'$ and $\Delta x = \Delta y \geq 0$ ⁵ characterize the source-observer separation geometry, $\tilde{a}_{P,n}$ is the (source distribution dependent) amplitude of the P th layer’s n th mode ($1 \leq P \leq N$), $\tilde{\mathbf{e}}_{P,n}$ and $\tilde{k}_{P,n}$ are the electric field vector and corresponding longitudinal propagation constant (resp.) of the n th mode in layer P arising from the components of the (source type, field type, and layer material-dependent) 3×3 spectral domain Green’s Tensor (e.g., see $\tilde{\mathbf{G}}_{ee}(\mathbf{k})$ and $\tilde{\mathbf{G}}_{em}(\mathbf{k})$ in (IV.3)-(IV.4)), and $u(\cdot)$ denotes the Heaviside step function. Similarly, $\mathcal{E}_s(\mathbf{r})$ is the scattered field contribution, due to the planar stratification, in layer L :

$$\mathcal{E}_s(\mathbf{r}) = \frac{i}{(2\pi)^2} \iint_{-\infty}^{+\infty} \left[(1 - \delta_{L,N}) \sum_{n=1}^2 \tilde{a}_{L,n}^s \tilde{\mathbf{e}}_{L,n} e^{i\tilde{k}_{L,n}z} + (1 - \delta_{L,1}) \sum_{n=3}^4 \tilde{a}_{L,n}^s \tilde{\mathbf{e}}_{L,n} e^{i\tilde{k}_{L,n}z} \right] \times e^{ik_x \Delta x + ik_y \Delta y} dk_x dk_y \quad (\text{II.6})$$

where $\tilde{a}_{P,n}^s$ is the scattering amplitude of the n th mode supported in layer P . In “monostatic”-like scenarios, where $|\mathbf{r}|$ approaches $|\mathbf{r}'|$, the magnitudes of both the direct field solution $\mathcal{E}_d(\mathbf{r})$ and the total field solution $\mathcal{E}(\mathbf{r}) = \delta_{L,M} \mathcal{E}_d(\mathbf{r}) + \mathcal{E}_s(\mathbf{r})$ become very large and (as noted before) would result in physically meaningless results if using post-integration direct field subtraction. Note that, as discussed in Section IV and illustrated explicitly in (IV.14)-(IV.15), the presence of a distributed (rather than Hertzian dipole) source simply acts as a multiplicative factor that augments the direct field (and, from causality considerations, the scattered field as well) modal amplitudes of a Hertzian dipole source. As a result, the remaining operations required to evaluate (II.5)-(II.6), as described in [32–34], are left untouched.

Before we proceed, a few observations are in order. When referring to the m th modal field in layer P as being “phase-referenced” to a particular $z = z_o$ plane, this means that its

⁵ An azimuthal coordinate rotation is assumed to have been performed to facilitate $\Delta x = \Delta y \geq 0$, and hence robust convergence of both the k_x and k_y spectral integrals [33, 34]. This rotation is assumed for all derivations done within the present paper.

longitudinal propagation constant has been cast in the form $e^{i\tilde{k}_{P,mz}(z-z_o)}$. When an isotropic layer P is discussed, the longitudinal propagator variables $\tilde{k}_{P,z}^+$ and $\tilde{k}_{P,z}^-$ may be used in place of the propagator values $\tilde{k}_{P,1z} = \tilde{k}_{P,2z} = \tilde{k}_{P,z}^+$ and $\tilde{k}_{P,3z} = \tilde{k}_{P,4z} = \tilde{k}_{P,z}^-$ (resp.). To simplify notation, modal or layer subscripts will be omitted on the longitudinal propagation constants whenever they are clear from the context. Finally, as detailed in [32], the numerical evaluation of the integrands appearing in (II.5)-(II.6) is predicated on computing the characteristic plane wave modes, the intrinsic and generalized reflection and transmission matrices, and the modal amplitudes [32][38, Ch.2].

III. DIRECT FIELD SUBTRACTION

A. Modal Field Representation Modifications

We now exhibit the formulation to extract the scattered electric field observed at \mathbf{r} in layer L due to a source at \mathbf{r}' in layer $M = L$ for $1 \leq (M = L) \leq N$. We use here same notation and nomenclature as [32], briefly reviewed next. First define $\tilde{\mathbf{a}}_D^+$ ($\tilde{\mathbf{a}}_D^-$) as the direct field 2×1 modal amplitude vector associated with up-going (down-going) characteristic modes in layer M phase-referenced to the top (bottom) bounding interface at depth z_{M-1} (z_M) [32]. Also define the 2×1 vectors $\tilde{\mathbf{a}}_{Sm}^+$ and $\tilde{\mathbf{a}}_{Sm}^-$ as the up-going and down-going scattered field modal amplitudes (resp.) in layer M , whose respective modal fields are phase-referenced to the interface at either $z = z_{M-1}$ (for $m = 1$) or $z = z_M$ (for $m = 2$) [32]. Further, denote the 2×2 generalized reflection matrix from layer m to adjacent layer n ⁶ as $\tilde{\tilde{\mathbf{R}}}_{m,n}$. One then obtains the standard formulae below for the scattered field amplitudes as a function of the direct field amplitudes [32]⁷:

$$\bar{\mathbf{\Lambda}}_M^+(z_o) = \text{diag} \left[e^{i\tilde{k}_{M,1z}z_o} \ e^{i\tilde{k}_{M,2z}z_o} \right], \quad \bar{\mathbf{\Lambda}}_M^-(z_o) = \text{diag} \left[e^{i\tilde{k}_{M,3z}z_o} \ e^{i\tilde{k}_{M,4z}z_o} \right] \quad (\text{III.1})$$

$$\tilde{\mathbf{M}}_1 = \bar{\mathbf{\Lambda}}_M^+(z_{M-1} - z_M) \cdot \tilde{\tilde{\mathbf{R}}}_{M,M+1}, \quad \tilde{\mathbf{M}}_2 = \bar{\mathbf{\Lambda}}_M^-(z_M - z_{M-1}) \cdot \tilde{\tilde{\mathbf{R}}}_{M,M-1} \quad (\text{III.2})$$

$$\tilde{\mathbf{a}}_{S1}^- = \left[\bar{\mathbf{I}}_2 - \tilde{\tilde{\mathbf{R}}}_{M,M-1} \cdot \tilde{\mathbf{M}}_1 \cdot \bar{\mathbf{\Lambda}}_M^-(z_M - z_{M-1}) \right]^{-1} \cdot \tilde{\tilde{\mathbf{R}}}_{M,M-1} \cdot \left[\tilde{\mathbf{a}}_D^+ + \tilde{\mathbf{M}}_1 \cdot \tilde{\mathbf{a}}_D^- \right] \quad (\text{III.3})$$

$$\tilde{\mathbf{a}}_{S2}^+ = \left[\bar{\mathbf{I}}_2 - \tilde{\tilde{\mathbf{R}}}_{M,M+1} \cdot \tilde{\mathbf{M}}_2 \cdot \bar{\mathbf{\Lambda}}_M^+(z_{M-1} - z_M) \right]^{-1} \cdot \tilde{\tilde{\mathbf{R}}}_{M,M+1} \cdot \left[\tilde{\mathbf{a}}_D^- + \tilde{\mathbf{M}}_2 \cdot \tilde{\mathbf{a}}_D^+ \right] \quad (\text{III.4})$$

⁶ That is, n equals either $m+1$ or $m-1$ when n corresponds to the layer below or above layer m , respectively,

where layer m is the layer containing the incident modal fields.

⁷ $\bar{\mathbf{I}}_n$ is the $n \times n$ identity matrix.

which are required when $M = L$. Then the observed scattered field amplitudes write as

$$\tilde{\mathbf{a}}_L^+ = \bar{\mathbf{\Lambda}}_L^+(z - z_L) \cdot \tilde{\mathbf{a}}_{S2}^+, \quad \tilde{\mathbf{a}}_L^- = \bar{\mathbf{\Lambda}}_L^-(z - z_{L-1}) \cdot \tilde{\mathbf{a}}_{S1}^- \quad (\text{III.5})$$

with the subsequent scattered amplitude-weighted superposition of the observed scattered modal fields following the prescription described in [32]. Note that if $M = L = 1$ or $M = L = N$, (III.3) or (III.4) (resp.) reduce to $\mathbf{0}$ and confirm the fact that no down-going or up-going reflected fields are present in layer L (resp.) [38][Ch. 2].

Now that the direct fields have served their purpose of exciting the scattered fields, their subtraction from the total field solution enters via coercion of the Kronecker delta $\delta_{L,M}$ in the expression $\mathcal{E}(\mathbf{r}) = \delta_{L,M} \mathcal{E}_d(\mathbf{r}) + \mathcal{E}_s(\mathbf{r})$ to zero. Indeed, one uses the direct-field amplitudes to excite the scattered fields, but does *not* include the direct field contributions themselves when assembling the total observed modal field for some (k_x, k_y) doublet, as evidenced by the expressions for $\tilde{\mathbf{a}}_L^+$ and $\tilde{\mathbf{a}}_L^-$ in (III.5) being devoid of *explicit* dependence on $\tilde{\mathbf{a}}_D^+$ and $\tilde{\mathbf{a}}_D^-$ ⁸. We emphasize that such an extraction procedure is independent of the type of excitation involved, i.e., it sports applicability to electric and (equivalent) magnetic currents of arbitrary polarization, (bounded) amplitude profile, and (compact) spatial support region. Finally, we remark that due to the concept of a “scattered” field becoming more ambiguous when $M \neq L$, the observed modal field amplitudes are computed identically to the procedure used in [32] to compute the *total* field.

B. Additional Remarks

The spectral integral in (II.6) is evaluated along properly chosen integration contours in the k_x and k_y complex planes. For details, the reader is referred to [33, 34].

Indeed, for geometries in which the source distribution’s height above the terrain far exceeds the transverse source-observer separation (such as in typical mono-static airborne or spaceborne radar scenarios), one can compute (II.6) using a trapezoidal detour in the propagating and weakly evanescent⁹ spectral zone [33, 34] followed by a real-axis integration of the semi-infinite Fourier integral “tail” (i.e., the strongly evanescent spectrum field contribution) using standard Gauss-Laguerre numerical quadrature. This is confirmed by referring

⁸ Implicitly, of course, these amplitudes do depend on the direct field excitation.

⁹ As noted in [34], no clear-cut definition or boundary, which would differentiate propagating and evanescent modes in the spectral domain, in general exists when anisotropy, loss, or material inhomogeneity exists.

Therefore, the terms “propagating spectra” and “evanescent spectra” are used here in a loose sense.

to Figure 2 and associated discussion of [33], and by noting the (conservative) estimate below of the effective longitudinal propagation distance z_{eff} traversed by the characteristic modes¹⁰ (see (III.6)). This reveals that the integration path's asymptotically optimal detour angle is approximately $\gamma = 0$ in such a scenario [33, 34, 52]. For more general geometries, one should revert to using the standard formula $\gamma = \tan^{-1}(|\Delta x/\Delta z|)$ [33], where one now replaces $\Delta z = z - z'$ with Δz_{eff} given by

$$\Delta z_{eff} = \begin{cases} |z - z'| & , M \neq L \\ (z - z_1) + (z' - z_1) & , M = L = 1 \\ (z_{N-1} - z) + (z_{N-1} - z') & , M = L = N \\ \min [(z_{M-1} - z) + (z_{M-1} - z'), (z - z_M) + (z' - z_M)] & , 1 < (M = L) < N \end{cases} \quad (\text{III.6})$$

In the first and fourth cases above, for which $M \neq L$ and $1 < (M = L) < N$ (resp.), one has (excepting when $M \neq L$ and $L = 1$ or N) both up-going and down-going scattered fields. Therefore, we are obliged to make conservative (small) assumptions for Δz_{eff} to minimize the residual¹¹ $\exp(r_x \cos \gamma_x \Delta z_{eff})$ that we add back into the integrand. Indeed, this is especially important due to the asymptotic Constant Phase Path (CPP), in general, not being well defined due to anisotropy and planar inhomogeneity [33, 34]. Therefore, conservatively assigning Δz_{eff} avoids situations where (for example) $1 < (M = L) < N$, the source and observation points are both very close to the interface at $z = z_{M-1}$, and one uses an alternative effective propagation distance such as $\Delta z_{eff} = [(2z_{M-1} - z - z') + (z + z' - 2z_M)]/2$ that may over-estimate the effective longitudinal propagation distance of the down-going scattered fields. This may lead to exponential kernels of the form¹² $\exp(i\tilde{k}_z^+ \Delta z' + \Delta z_{eff} r_x \cos \gamma_x)$, corresponding to the down-going scattered fields whose actual effective longitudinal propagation distance has been overestimated as Δz_{eff} . Such exponential residuals may lead to unbounded solutions for increasing $|r_x|$, rather than asymptotically tending to a constant magnitude and contributing towards a numerically stable computation process [34].

¹⁰ Note that for problems with more than two layers, wherein both up-going direct *and* scattered modes can produce down-going modes (and vice versa), a true longitudinal propagation distance cannot be defined. Rather, “effective” longitudinal propagation distance here represents a conservative estimate of the distance traversed by the scattered fields.

¹¹ r_x is the real-valued variable in [34] in terms of which the k_x plane integration contour path “tail” is parameterized. The residual factor $\exp(\Delta z_{eff} r_x \cos \gamma_x)$ arises from using complex-plane Gauss-Laguerre quadrature. An analogous definition exists for r_y and k_y plane integration. See [34] for details.

¹² $\Delta z'$ in these expressions is used loosely to denote the mode-dependent effective longitudinal distance.

C. Validation Results: Scattered Field Extraction

To validate the algorithm’s ability to accurately extract the scattered field, we use it to verify the following well-known results concerning the effect of placing Hertzian dipole radiators close to a perfectly conducting ground plane of infinite lateral extent [51]:

1. The direct EM field of a vertical electric dipole (VED) will be reinforced by the field scattered off the ground. That is, the scattered and direct fields should be equal.
2. The direct EM field of a vertical magnetic dipole (VMD) will be canceled by the ground-scattered field. That is, the scattered and direct contributions to any given field component should be equal in magnitude and opposite in sign.

To avoid (1) numerical instability due to entering an infinite conductivity for the ground plane and (2) inaccuracy stemming from a ground plane with finite conductivity, the presence of a perfectly reflecting ground plane is equivalently effected via manually coercing, within the code, the ground plane’s intrinsic reflection coefficients for the incident TE_z and TM_z modes [32]. We emphasize that this coercion is done only to facilitate the present image theory study and does not fundamentally alter any of the other computations.

Prior to discussing results, we note the following conventions used for all numerical results discussed in the paper: (1) All errors are displayed as field component-wise relative error $10\log_{10}|(L_{num} - L_{exact})/L_{exact}|$ (dB units); (2) all computations are performed in double precision; (3) any relative errors below -150dB are coerced to -150dB; (4) An adaptive integration tolerance of 1.2×10^n denotes a precision goal of approximately n digits; and (5) the error is coerced to -150dB whenever the computed and reference solution magnitudes are (within machine precision equal to) zero.

Figure 2a shows the error in computing the reflected electric field E_z due to a VED, while Figure 2b shows the error in computing the reflected magnetic field H_z due to a VMD, where both sources are radiating at $f=2\text{MHz}$. The observation point is kept at a fixed radial distance $r=10\text{m}$ from the source, the observation angle in azimuth is set to $\phi = 0^\circ$, and the polar angle θ is swept from $-89^\circ \leq \theta \leq 89^\circ$. To test the scattered-field extraction for all possible scenarios concerning the source and observation points being in the same layer¹³, we perform the scattered-field extraction in the following four cases referred to in the legends of

¹³ Recall that if the source and observation layers differ, the algorithm recovers the total field.

Figures 2a-2b. Case 1: Vacuum half-space above perfect electric conductor (PEC) half-space, with the source placed above ground. Case 2: Vacuum half-space below PEC half-space, with the source placed below ground. Case 3: Vacuum half-space, fictitiously partitioned into two layers such that both source and observer reside in a “slab” of vacuum, above PEC half-space (source placed above ground). Case 4: Vacuum half-space, fictitiously partitioned into two layers such that both source and observer reside in a “slab” of vacuum, below PEC half-space (source placed below ground). The distance of the source to the ground is set to 1.0×10^{-15} m. Needless to say, this distance (nuclear scale) is many order of magnitudes below the length scales of this problem; rather, it is simply used as a numerical means to test the proposed scattered-field extraction algorithm’s accuracy.

We observe that approximately between the angles $-60^\circ \leq \theta \leq 60^\circ$ the algorithm delivers at least eleven digits of accuracy, which is consistent with the adaptive integration tolerance set as 1.2×10^{-12} , with accuracy declining to approximately four digits as the observation point tends toward the surface of the ground plane. The cause behind this degradation of accuracy as the polar observation angle tends towards horizon, which is also evident in the wire and aperture antenna studies in Sections IV E and IV F below, is a topic of ongoing investigation.

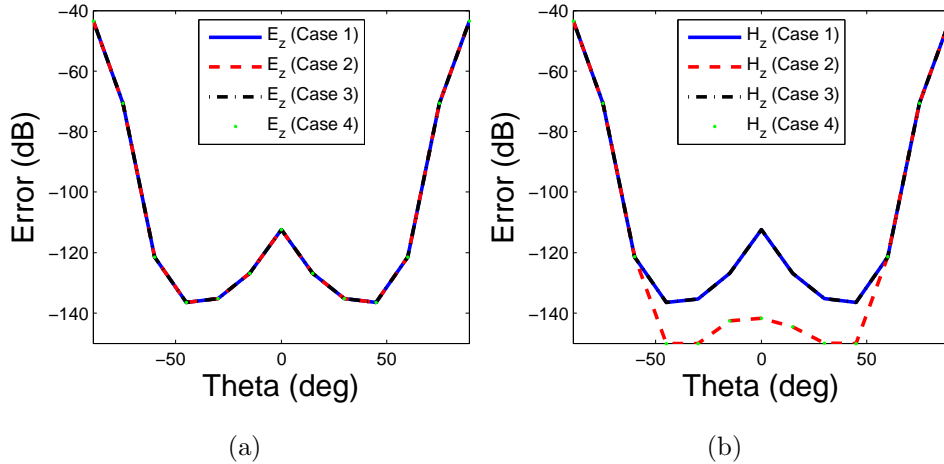


FIG. 2: Error in computing the field reflected off of the ground plane. For the VED and VMD cases, the reference field results are E_z and $-H_z$ in homogeneous vacuum (resp.).

IV. DISTRIBUTED-SOURCE FIELD COMPUTATION

A. Introduction

The importance of efficiently evaluating fields radiated by distributed sources manifests in scenarios such as (1) simulating the radiated fields from antenna geometries modeled to more closely resemble practical antenna geometries or (2) utilizing a forward engine in an aperture synthesis procedure to design arrayed and reflector antennas [53, 54], where in either case one may wish to analyze and (or) compensate, in the antenna design, for the effects of layered, absorptive, anisotropic media on EM wave propagation concerning the radiator of interest. This process traditionally involves discretization of the radiation integrals concerning the electric field produced by either an electric or (equivalent) magnetic current source distribution (resp.):

$$\mathcal{E}(\mathbf{r}) = ik_0\eta_0 \iiint_{V'} \bar{\mathcal{G}}_{ee}^s(\mathbf{r}; \mathbf{r}') \cdot \mathcal{J}(\mathbf{r}') dV' \quad (\text{IV.1})$$

$$\mathcal{E}(\mathbf{r}) = - \iiint_{V'} \bar{\mathcal{G}}_{em}^s(\mathbf{r}; \mathbf{r}') \cdot \bar{\boldsymbol{\mu}}_r^{-1}(\mathbf{r}') \cdot \mathcal{M}(\mathbf{r}') dV' \quad (\text{IV.2})$$

where $\bar{\mathcal{G}}_{ee}^s(\mathbf{r}; \mathbf{r}')$ and $\bar{\mathcal{G}}_{em}^s(\mathbf{r}; \mathbf{r}')$ are the space domain (scattered-field) tensor Green's functions and $dV' = dx'dy'dz'$ is the differential volume element on the emitter antenna manifold occupying region V' in layer M . Now admit either an electric *or* magnetic source distribution and assume it is contained in one layer for simplicity. Furthermore, let N_{avg} denote the average number of points on V' whose equivalent Hertzian dipole contributions, to the electric field at observation point \mathbf{r} , need to be sampled to re-construct the observed field with some pre-prescribed accuracy level. In this case, one must (in general) evaluate a total of N_{avg} two-dimensional Fourier integrals due to the space domain tensor Green's functions being translation-*variant* along the longitudinal direction. In addition, one must then evaluate the space domain radiation integrals (IV.1)-(IV.2) themselves, which for an electrically large radiator with rapid variation in the current amplitude and/or polarization profile may itself also be a non-trivial task. It turns out that for simple antenna geometries whose space-domain Fourier transforms are readily available in closed form, one can feasibly eliminate the intermediate step of evaluating the radiation integrals in (IV.1)-(IV.2) by directly computing the radiation integrals in the spectral domain itself. Indeed, for a homogeneous medium

(IV.1)-(IV.2) reduce to three-dimensional convolution integrals which can equivalently be computed in the Fourier domain:

$$\mathcal{E}(\mathbf{r}) = ik_0\eta_0 \left(\frac{1}{2\pi}\right)^3 \iiint_{-\infty}^{\infty} \tilde{\mathbf{G}}_{ee}(\mathbf{k}) \cdot \tilde{\mathbf{J}}(\mathbf{k}) e^{ik_x(x-x') + ik_y(y-y') + ik_z(z-z')} dk_x dk_y dk_z \quad (\text{IV.3})$$

$$\mathcal{E}(\mathbf{r}) = - \left(\frac{1}{2\pi}\right)^3 \iiint_{-\infty}^{\infty} \tilde{\mathbf{G}}_{em}(\mathbf{k}) \cdot \bar{\boldsymbol{\mu}}_r^{-1} \cdot \tilde{\mathbf{M}}(\mathbf{k}) e^{ik_x(x-x') + ik_y(y-y') + ik_z(z-z')} dk_x dk_y dk_z \quad (\text{IV.4})$$

whose more generalized manifestation, in the case of planar-layered media, writes as shown in (II.5)-(II.6). As shown below, the Fourier domain implementation can reduce the computational effort considerably; one or two orders of magnitude reduction in computation time for simulating wire or aperture antenna radiation (resp.) were realized in our numerical experiments, for example. Of course, in the case of homogeneous isotropic media, the spectral-domain implementation may not be advantageous since the space-domain tensor Green's functions are available in closed form [38, Ch. 1,7]. However, in either homogeneous media exhibiting arbitrary anisotropy or planar-stratified media as considered here, wherein space-domain tensor Green's functions are typically unavailable in closed form, the spectral domain evaluation of the radiation integrals offers a significant advantage.

B. Generalized Source Distribution: Formulation and Analyticity Considerations

First we start with the vector wave equation (II.2) under the assumption of a homogeneous medium, as usual. Assuming the source distribution to have a valid FT, i.e., $\tilde{\mathbf{J}}(\mathbf{k})$ and $\tilde{\mathbf{M}}(\mathbf{k})$ are well-defined spectral quantities, one can exhibit the spectral-domain version of (II.2) as

$$\tilde{\tilde{\mathbf{A}}}(\mathbf{k}) \cdot \tilde{\mathbf{E}}(\mathbf{k}) = ik_0\eta_0 \tilde{\mathbf{J}}(\mathbf{k}) - \tilde{\nabla} \times \bar{\boldsymbol{\mu}}_r^{-1} \cdot \tilde{\mathbf{M}}(\mathbf{k}) \quad (\text{IV.5})$$

Inverting $\tilde{\tilde{\mathbf{A}}}(\mathbf{k})$ and taking the three-dimensional inverse Fourier integral on both sides of (IV.5) yields the space domain electric field $\mathcal{E}(\mathbf{r})$. For a homogeneous medium, we note that (II.5) (with \mathcal{L} and $\tilde{\mathbf{L}}$ replaced by \mathcal{E} and $\tilde{\mathbf{E}}$ in (II.4), resp.) is just the spectral-domain implementation of convolution for a general source distribution (IV.3)-(IV.4). Despite the conceptually straightforward task of computing the radiation integral in the spectral domain, the presence of a *distributed* source presents a practical challenge to the numerically robust and stable evaluation of the EM field. This is because the analyticity properties of the

spectral integrand in regards to the k_x , k_y , and k_z spectral variables in (II.4) are now obfuscated. That is, one often encounters the following scenario with distributed radiators: Regardless of whether one deforms the integration path into the upper- or lower-half of the k_x or k_y complex plane, one may encounter a numerically overflowed result. To illustrate this, let us consider the modified FT pair below for the electric source current distribution $\mathcal{J}(\mathbf{r})$:

$$\tilde{\mathbf{J}}(\mathbf{k}) = \mathcal{F}\left\{\mathcal{J}(\mathbf{r})\right\} = \iiint_{-\infty}^{\infty} \mathcal{J}(\mathbf{r}') e^{-i\mathbf{k}\cdot\mathbf{r}'} d\mathbf{r}' \quad (\text{IV.6})$$

$$\mathcal{J}(\mathbf{r}) = \mathcal{F}^{-1}\left\{\tilde{\mathbf{J}}(\mathbf{k})\right\} = \left(\frac{1}{2\pi}\right)^3 \iiint_{-\infty}^{\infty} \iiint_{-\infty}^{\infty} \tilde{\mathbf{J}}(\mathbf{k}) e^{i\mathbf{k}\cdot\mathbf{r}} dk_x dk_y dk_z \quad (\text{IV.7})$$

where one can draw a physical association between \mathbf{r} and the observation point, as well as between \mathbf{r}' and an equivalent Hertzian dipole source in the support of \mathcal{J} . Now, assume fixed x and x' values for which one evaluates the inner (i.e., along k_x) spectral integral. One promptly realizes that depending on whether $(x - x') > 0$ or $(x - x') < 0$ the region of analyticity of the integrand, and hence the region in which one can apply Jordan's lemma in the k_x plane, depends on the sign of $x - x'$. Physically, this corresponds to a situation of the observer witnessing incoming radiation from sources at opposite directions along x . An analogous observation can be made w.r.t to distributed sources, along y and z , obfuscating the integrand's analyticity properties in the k_y and k_z planes (resp.). This issue can be exemplified by considering the simple case of two vertical Hertzian electric dipoles spaced L meters apart along the x axis, i.e., $\mathcal{J}(\mathbf{r}) = [\delta(x - L/2) + \delta(x + L/2)] \delta(y) \delta(z) \hat{\mathbf{z}}$, where $\delta(x)$ is the Delta Dirac function. Indeed, procuring the current distribution's three-dimensional FT $\tilde{\mathbf{J}}(\mathbf{k}) = [e^{-ik_x L/2} + e^{ik_x L/2}] \hat{\mathbf{z}} = 2\hat{\mathbf{z}} \cos(k_x L/2)$, (analytically) evaluating the k_z integral of the spectral field, and detouring in the k_x -plane integration path's "tail" section [33, 34] results in a spectral-domain source distribution $\tilde{\mathbf{J}}(\mathbf{k})$ whose magnitude grows without bound as $|\text{Im}(k_x)| \rightarrow \infty$ when $|x| < L/2$. Indeed, when $|x| < L/2$ one has $(x - x') > 0$ for one dipole source and $(x - x') < 0$ for the other dipole source; see Figure 3.

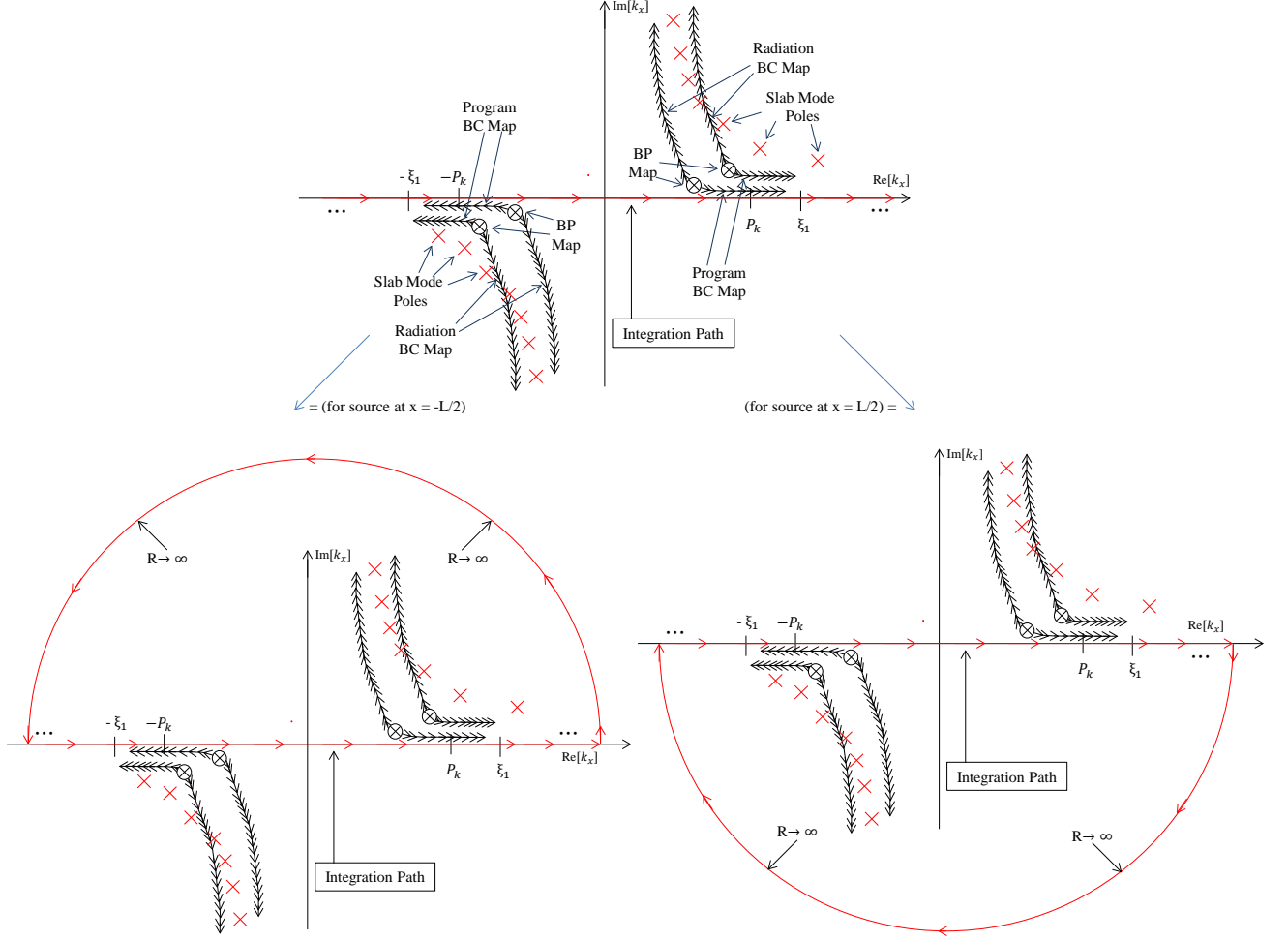


FIG. 3: Source-location-dependent region of analyticity of the spectral EM field in the k_x plane regarding the discussed example of two dipole sources. When $|x| < L/2$, the real-axis path is equivalent to enclosing either the upper-half or lower-half $\text{Im}[k_x]$ plane for the source located at $x' = -L/2$ or $x' = +L/2$ (resp.). See Figure 2 of [33] for definitions of the features and variables shown in Figure 3.

To remove the risk of numerical overflow for arbitrary \mathbf{r} , we make the conservative judgment to only allow observation of the *scattered* fields. To further suppress any exponentially rising terms, we purposefully incorporate the real-valued, numerical Laguerre-Gauss quadrature weights¹⁴ directly into the power of the complex exponentials prior to evaluating the exponentials themselves. Referring again to the notation and terminology used in [34], letting w_x be the Laguerre quadrature weight multiplying into the evaluation of the integrand

¹⁴ The constant, complex valued factors l^+ and l^- manifest in the expressions $k_x = l^\pm r_x \pm \xi_1$ used to parameterize the linear path deformation, appearing in Eqs. (2.10)-(2.11) of [34], are placed outside the double Fourier integral and thus allow the weights to be real-valued. See [34] for details.

for some (k_x, k_y) doublet $(k_{x0} = \xi_1 + l^+ r_{x0}, k_{y0})$, and (for the sake of illustration) assuming one is presently integrating in the intersection of the a) evanescent spectrum zone of the k_x plane (let $\text{Re}[k_x] > 0$) and b) propagation spectrum zone of the k_y plane, then upon defining

$$\tau = i\tilde{k}_z^+ \Delta z_{\text{true}} + r_{x0} \cos(\gamma_x)(i\Delta x + \Delta z_{\text{eff}}) + ik_{y0}\Delta y \quad (\text{IV.8})$$

for our twin vertical electric dipole radiation example, one can simply set

$$(e^{ik_{x0}L/2} + e^{-ik_{x0}L/2}) e^\tau w_x w_y \rightarrow (e^{ik_{x0}L/2 + \tau + \text{Log}(w_x)} + e^{-ik_{x0}L/2 + \tau + \text{Log}(w_x)}) w_y \quad (\text{IV.9})$$

where Log stands for the natural logarithm and \tilde{g} is some component of the spectral-domain tensor Green's function. Similarly, if one detours in the upper-half k_y plane to evaluate the plane wave spectra evanescent with respect to k_y , then place the k_y plane Laguerre-Gauss quadrature weight $\text{Log}(w_y)$ into the exponentials. Detouring into both the k_x and k_y upper-half planes, by extension, mandates placing $\text{Log}(w_x)$ and $\text{Log}(w_y)$ into both exponentials. Now we exhibit the explicit spectral-domain representation of two commonly encountered distributed source geometries, the linear (wire) and rectangular aperture antennas.

C. Linear Antennas

We consider a linear wire antenna of length L centered at $\mathbf{r}'_o = \mathbf{0}$ whose current distribution can be written, without loss of generality, as a superposition of harmonic current modes as follows [51]:

$$\mathcal{J}(\mathbf{r}) = \hat{\mathbf{z}}\delta(x)\delta(y)\text{rect}\left(\frac{z}{L}\right) \sum_{n=1}^{\infty} \left[J'_c(2n-1) \cos\left(\frac{(2n-1)\pi z}{L}\right) + J'_s(2n) \sin\left(\frac{2\pi n z}{L}\right) \right] \quad (\text{IV.10})$$

where J'_c and J'_s are the complex-valued modal current amplitudes. The unit pulse function is defined as $\text{rect}(u) = 1$ for $|u| < 1/2$ and zero otherwise. It is a simple exercise to show that

$$\tilde{\mathbf{J}}(\mathbf{k}) = \frac{-n\hat{\mathbf{z}}}{L} \sum_{n=1}^{\infty} \left[\frac{\xi_n J'_c(2n-1) \cos\left(\frac{k_z L}{2}\right) + i\xi'_n J'_s(2n) \sin\left(\frac{k_z L}{2}\right)}{(k_z - \frac{n\pi}{L})(k_z + \frac{n\pi}{L})} \right] \quad (\text{IV.11})$$

with

$$\xi_n = \begin{cases} 1, & n = 1, 5, 9, \dots \\ -1, & n = 3, 7, 11, \dots \\ 0, & \text{else} \end{cases}, \xi'_n = \begin{cases} -1, & n = 2, 4, 6, \dots \\ 1, & n = 4, 8, 12, \dots \\ 0, & \text{else} \end{cases} \quad (\text{IV.12})$$

Now let the wire antenna be oriented along an *arbitrary* direction $\hat{\mathbf{a}}$ relative to the (x, y, z) system (i.e., $\hat{\mathbf{z}}$ relative to the now-rotated antenna system) and with $J_c = J'_c \delta(\dot{x}) \delta(\dot{y})$ and $J_s = J'_s \delta(\dot{x}) \delta(\dot{y})$, where $\dot{\mathbf{r}} = (\dot{x}, \dot{y}, \dot{z})$ and $\dot{\mathbf{k}} = (\dot{k}_x, \dot{k}_y, \dot{k}_z)$ represent the position and wave vectors (resp.) in the antenna's local coordinates. To effect the spectral-domain current's representation in the original (x, y, z) system, one can use polar and azimuthal rotation angles α and β (resp.), along with their respective individual rotation matrices

$$\bar{\mathbf{U}}_\alpha = \begin{pmatrix} \cos \alpha & 0 & \sin \alpha \\ 0 & 1 & 0 \\ -\sin \alpha & 0 & \cos \alpha \end{pmatrix}, \quad \bar{\mathbf{U}}_\beta = \begin{pmatrix} \cos \alpha & -\sin \alpha & 0 \\ \sin \alpha & \cos \alpha & 0 \\ 0 & 0 & 1 \end{pmatrix} \quad (\text{IV.13})$$

and the composite rotation matrix $\bar{\mathbf{U}} = \bar{\mathbf{U}}_\beta \cdot \bar{\mathbf{U}}_\alpha$. Having defined these rotation matrices, we observe that $\dot{\mathbf{k}}$ and $\dot{\mathbf{r}}$ transform as $\mathbf{k} = \bar{\mathbf{U}} \cdot \dot{\mathbf{k}}$ and $\mathbf{r} = \bar{\mathbf{U}} \cdot \dot{\mathbf{r}}$, resp.

Now we comment on some features the resulting spectral-domain integral solution. Using Cauchy's Integral Theorem, the m th modal direct field residue ($m=1,2,3,4$) writes as¹⁵:

$$\tilde{a}_m \tilde{\mathbf{e}}_m = 2\pi i \left[\left(k_z - \tilde{k}_{mz} \right) i k_0 \eta_0 \text{Adj} \left(\tilde{\tilde{\mathbf{A}}} \right) \cdot \tilde{\mathbf{J}}(\mathbf{k}) e^{i k_z z} / \text{Det} \left(\tilde{\tilde{\mathbf{A}}} \right) \right] \Big|_{k_z = \tilde{k}_{mz}} \quad (\text{IV.14})$$

for an arbitrary electric source distribution. The particular case of a vertically-oriented electric linear antenna centered at $\mathbf{r}'_o = (x_o, y_o, z_0)$ reads as

$$\tilde{a}_m \tilde{\mathbf{e}}_m = 2\pi k_0 \eta_0 \text{Adj} \left(\tilde{\tilde{\mathbf{A}}} \right) \cdot \hat{\mathbf{z}} e^{i k_z z - i \mathbf{k} \cdot \mathbf{r}'_o} \left(k_z - \tilde{k}_{mz} \right) \times \sum_{n=1}^{\infty} \left[n \frac{\xi_n J'_c(2n-1) \cos \left(\frac{k_z L}{2} \right) + i \xi'_n J'_s(2n) \sin \left(\frac{k_z L}{2} \right)}{L \left(k_z - \frac{n\pi}{L} \right) \left(k_z + \frac{n\pi}{L} \right)} \right] \Big|_{k_z = \tilde{k}_{mz}} \quad (\text{IV.15})$$

where the entire expression for $\tilde{a}_m \tilde{\mathbf{e}}_m$ (not just the bracketed portion) is subject to evaluation at a particular eigenvalue \tilde{k}_{mz} . As can be observed in (IV.14)-(IV.15), the distributed source spectrum simply acts as a multiplicative ‘‘taper’’ of the computed direct field modal amplitudes of a Hertzian dipole (see [32] for these latter computation details), leaving the other fundamental modal field computations and integration process outlined in [32–34] unchanged. Finally, we should note that despite the factor $(k_z - n\pi/L)(k_z + n\pi/L)$ in the denominator of $\tilde{\mathbf{J}}(\mathbf{k})$ in (IV.11) and (IV.15), the points $k_z = \pm n\pi/L$ are *not* poles because of the zeros in the numerator at those same points [56].

¹⁵ Note that $\text{Adj}(\bar{\mathbf{M}})$ is the adjugate (not adjoint) of matrix $\bar{\mathbf{M}}$ [55], and $\text{Det}(\bar{\mathbf{M}})$ is the determinant.

D. Aperture Antennas

Now consider a rectangular aperture possessing a tangential EM field distribution on its plane that one recasts, via the equivalence theorem, as a tangentially-polarized, surface-confined, magneto-electric current distribution [51]. Assuming the aperture's (1) principal axes are parallel with the x and y axes with principal lengths L_x and L_y (resp.) and (2) central location is $\mathbf{r}'_o = \mathbf{0}$, its spectral-domain representation readily follows from (IV.11) upon letting m and n be the modal current indices describing current amplitude oscillation along x and y (resp.). However, unlike the linear antenna supporting a physical current that must vanish at the wire's ends, there are no such restrictions on the aperture's equivalent currents. Therefore, there may be both sinusoidal and cosinusoidal modal variations for each modal index $m > 0$ and modal index $n > 0$ in addition to a "DC" term comprising a constant current amplitude sheet. Letting $J'_{a,p,q}(m,n)$ stand for the (possibly complex-valued) Fourier coefficient of a current mode with (1) constant current direction $\hat{\mathbf{a}}$ ($a=x$ or y), (2) either sinusoidal ($p=s$) or cosinusoidal ($p=c$) current variation along the x direction, and (3) either sinusoidal ($q=s$) or cosinusoidal ($q=c$) current variation along the y direction, then upon defining the sub-expressions

$$\tau(\mathbf{r}) = \text{rect}\left(\frac{x}{L_x}\right)\text{rect}\left(\frac{y}{L_y}\right)\delta(z) \quad (\text{IV.16})$$

$$\mathcal{J}_1(m,n)(\mathbf{r}) = \tau(\mathbf{r}) \left[\hat{\mathbf{x}} J'_{x,s,s}(m,n) \sin \frac{m\pi x}{L_x} \sin \frac{n\pi y}{L_y} + \hat{\mathbf{y}} J'_{y,s,s}(m,n) \sin \frac{m\pi x}{L_x} \sin \frac{n\pi y}{L_y} \right] \quad (\text{IV.17})$$

$$\mathcal{J}_2(m,n)(\mathbf{r}) = \tau(\mathbf{r}) \left[\hat{\mathbf{x}} J'_{x,s,c}(m,n) \sin \frac{m\pi x}{L_x} \cos \frac{n\pi y}{L_y} + \hat{\mathbf{y}} J'_{y,s,c}(m,n) \sin \frac{m\pi x}{L_x} \cos \frac{n\pi y}{L_y} \right] \quad (\text{IV.18})$$

$$\mathcal{J}_3(m,n)(\mathbf{r}) = \tau(\mathbf{r}) \left[\hat{\mathbf{x}} J'_{x,c,s}(m,n) \cos \frac{m\pi x}{L_x} \sin \frac{n\pi y}{L_y} + \hat{\mathbf{y}} J'_{y,c,s}(m,n) \cos \frac{m\pi x}{L_x} \sin \frac{n\pi y}{L_y} \right] \quad (\text{IV.19})$$

$$\mathcal{J}_4(m,n)(\mathbf{r}) = \tau(\mathbf{r}) \left[\hat{\mathbf{x}} J'_{x,c,c}(m,n) \cos \frac{m\pi x}{L_x} \cos \frac{n\pi y}{L_y} + \hat{\mathbf{y}} J'_{y,c,c}(m,n) \cos \frac{m\pi x}{L_x} \cos \frac{n\pi y}{L_y} \right] \quad (\text{IV.20})$$

one has the following expression for the equivalent aperture currents in the space domain:

$$\mathcal{J}(\mathbf{r}) = \mathcal{J}_4(0,0)(\mathbf{r}) + \sum_{m=1}^{\infty} \sum_{n=1}^{\infty} \sum_{p=1}^4 \mathcal{J}_p(m,n)(\mathbf{r}) \quad (\text{IV.21})$$

with associated spectral-domain representation

$$\tilde{\mathbf{J}}(\mathbf{k}) = \tilde{\mathbf{J}}_4(0, 0)(\mathbf{k}) + \sum_{m=1}^{\infty} \sum_{n=1}^{\infty} \sum_{p=1}^4 \tilde{\mathbf{J}}_p(m, n)(\mathbf{k}) \quad (\text{IV.22})$$

Analogous to the linear antenna, a more general aperture plane orientation can be effected using the rotation matrices and procedure discussed above for arbitrarily-oriented wire antennas. Akin to the wire antenna case, we observe again the manifestation of (1) a tapering in the field's Fourier spectrum (except now along both k_x and k_y), (2) the property of the distributed field computation only imparting a simple multiplicative factor into the computed Hertzian dipole direct field modal amplitudes, (3) the presence of (now four) fictitious poles, and (4) the vulnerability of numerical instability when the observation point lies within the region $(|x| < L_x/2) \cup (|y| < L_y/2)$. The latter instability aspect, when one is detouring into the upper-half k_x and k_y planes, is mitigated in the same manner to that shown concerning linear antennas, i.e., via placing the natural logarithm of one or both of the Laguerre-Gauss quadrature weights into the exponentials prior to evaluating them, as well as evaluating the scattered fields. Now, however, due to the multiplication of two sinusoid-type functions in the spectral domain one will have for each current mode functional dependance (i.e., cosinusoidal along both x and y , sinusoidal along both x and y , etc.) four exponentials into which one places the quadrature weights, rather than two in the case of wire antennas.

E. Validation Results: Linear Antennas

We now show results concerning the fields radiated by an infinitesimally thin linear antenna radiating at $f=30\text{MHz}$ in unbounded free space. To facilitate comparison against a reference result whose closed form solution is known [51], we (1) keep the wire antenna's length at half the free space wavelength (wire length $L = \lambda_0/2 \sim 5\text{m}$) while partitioning free space into three fictitious layers, with the antenna in the 5m-thick central layer and the observation point always either in the top or bottom layer to compute the total field and (2) restrict attention to an electric current distribution with mode index $n = 1$. Furthermore, whenever both the algorithm and closed form solution yield field values having magnitudes that are within machine precision of zero, the error is coerced to -150dB. Finally, note that the radial distance between the antenna's center and all observation points is held fixed at $r = 50\text{m}$, while the adaptive integration error tolerance was set to be 1.2×10^{-4} .

Figure 5 shows the accuracy of the electric field, radiated by a vertically-oriented wire antenna (see Figure 4a for a schematic pictorial description), versus polar angle θ for a fixed azimuthal observation angle $\phi = 0^\circ$. Note that for $r = 50\text{m}$ the polar angles $\theta = 88^\circ$, 90° , and 92° correspond to observation points lying within the central free space layer and thus zero scattered-field result. Thus, the polar angle sweep data is shown sub-divided into two plots to remove the artificial discontinuity in the data (versus θ) due to the nature of the scattered-field algorithm. We see that between $\theta = 0^\circ - 76^\circ$ and $\theta = 104^\circ - 180^\circ$, one realizes an accuracy of between thirteen to fourteen digits in E_z . An analogous statement applies for the error in E_x except at $\theta = 0^\circ$ and $\theta = 180^\circ$, where the algorithm's computed solution (to within machine precision) and closed form solution yield answers for E_x having magnitude equal to zero (hence the error's coercion to -150dB). We notice that the accuracy degrades as the polar observation angle tends towards horizon, but the algorithm still manages to deliver results accurate to approximately four digits. This trend is qualitatively consistent with the results in Section III C, where instead the field and observation points were in the same layer.

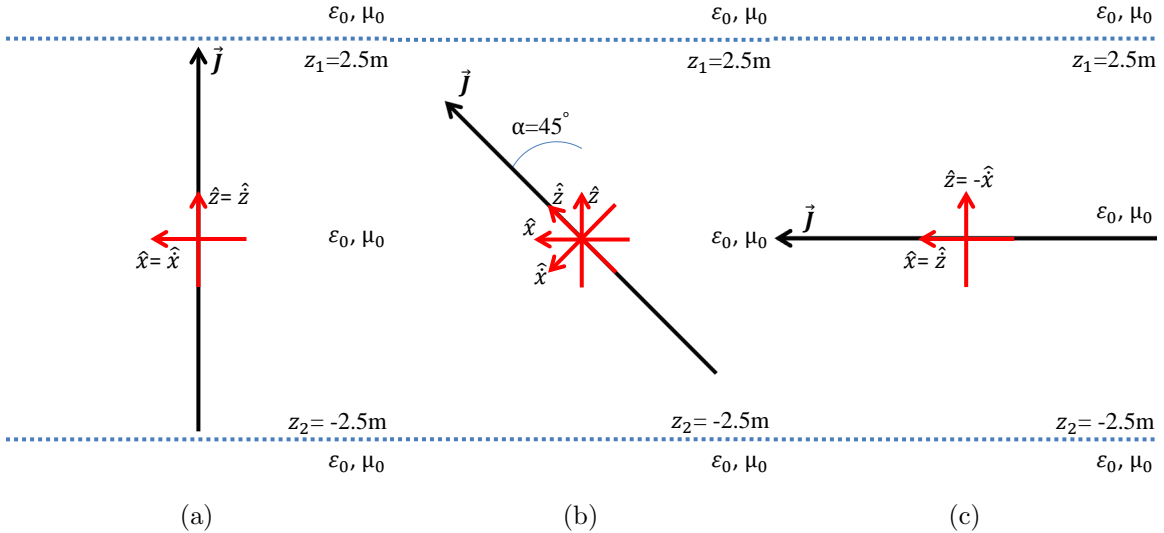


FIG. 4: Schematic depiction of the three wire antenna orientation scenarios examined. In Figures 4a, 4b, and 4c the wire antenna is tilted by a polar angle of $\alpha = 0^\circ$, $\alpha = 45^\circ$, and $\alpha = 90^\circ$ with respect to the z axis (resp.), with azimuth tilt angle $\beta = 0^\circ$.

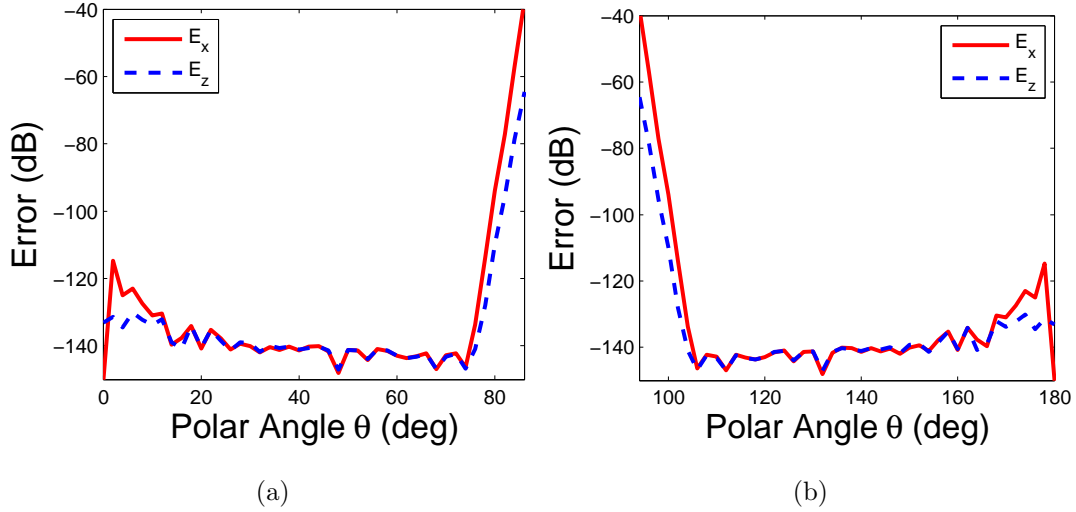


FIG. 5: Accuracy of computed electric field components, versus polar angle θ , for the wire antenna.

Now we show validation results concerning the algorithm's accuracy computing the magnetic field \mathcal{H} radiated by obliquely-oriented wire antennas, which is summarized in Table I. We see that agreement between the algorithm's results and closed-form solutions shows at least thirteen digits of accuracy. Further extensive error studies were also performed to better characterize the algorithm's performance, which consisted of all the following parameter permutations: $(E_{\dot{x}}, E_{\dot{y}}, E_{\dot{z}}, H_{\dot{x}}, H_{\dot{y}}) \times (\alpha = 0^\circ, \alpha = 45^\circ, \alpha = 90^\circ) \times (\theta = 45^\circ, \theta = 135^\circ) \times (\phi = 0^\circ, \phi = 45^\circ, \phi = 90^\circ, \phi = 135^\circ, \phi = 180^\circ, \phi = 225^\circ, \phi = 270^\circ, \phi = 315^\circ)$. The results in all these permutations are similar to that shown in Table I. The dot over the field component directions denotes components expressed w.r.t. the antenna's local (rotated) coordinate system.

Based on comparing the computational time required to obtain the solution (for same accuracy) using the present spectral-domain approach against a conventional (space-domain integration) approach in performed numerical experiments, a factor or approximately one order of magnitude in acceleration is realized¹⁶. Two main reasons contribute to this acceleration: (1) efficiency in representing the current distribution since Fourier current modes constitute a far sparser representation of the current [51] compared to having to finely sample

¹⁶ For the space domain approach, we do not include the time required to perform the evaluation of the radiation integral (IV.1) since its evaluation time is (relatively) much smaller than the time required to actually obtain the electric field contributions from each equivalent Hertzian dipole source on the current manifold V' .

in space and (2) the tapering effect imparted onto the field's spectral-domain spectrum (c.f. (IV.15) and (IV.22)), leading to accelerating the convergence of the numerical integration in the spectral domain.

TABLE I: Relative Error of Magnetic Field $\epsilon(\mathcal{H})$: $\theta = 45^\circ$

α (deg)	ϕ (deg)	$\epsilon(H_{\hat{x}})$ (dB)	$\epsilon(H_{\hat{y}})$ (dB)
45	0	-150	-150
45	45	-137	-137
45	90	-142	-142
45	135	-142	-142
45	180	-150	-141
45	225	-142	-142
45	270	-142	-142
45	315	-137	-138
90	0	-150	-140
90	45	-144	-144
90	90	-139	-139
90	135	-142	-142
90	180	-150	-139
90	225	-144	-144
90	270	-139	-139
90	315	-142	-142

Relative error of \mathcal{H} versus α and ϕ . Adaptive error goal was set to 1.2×10^{-4} .

F. Validation Results: Aperture Antennas

Now we exhibit validation results concerning rectangular aperture antennas radiating at $f=30\text{MHz}$ in free space. To again facilitate comparison against a reference result, we (1) assume the aperture antenna's dimensions along the principal directions equal to half the free space wavelength ($L = L_x = L_y = \lambda_0/2$) while partitioning free space into three fictitious layers, with the antenna in the central layer (2m thickness in Figure 6 and 5m thickness in

Table II) and the observation point always either in the top or bottom layer to compute the direct field, (2) restrict attention to the lowest-order mode ($m, n = 1$) when dealing with cosinusoidal electric current variation along one or both of the principal aperture plane directions, and (3) assume cosinusoidal current variation along the direction of current flow. With these assumptions, one can easily and rigorously compute the closed-form solution to the space domain aperture current distribution via evaluation of a convolution integral concerning the field radiated by a linear superposition of half-wavelength wire antennas [51, 56].

Figure 6 shows the accuracy of the electric field, radiated by an aperture antenna with area normal $\hat{\mathbf{n}} = \hat{\mathbf{z}}$ and centered at $\mathbf{r}'_0 = \mathbf{0}$, versus polar angle θ for a fixed azimuthal observation angle $\phi = 0^\circ$. The radial distance between the center of the aperture and all observation points is held fixed at $r = 50\text{m}$, while the adaptive integration error tolerance was set to be 1.2×10^{-4} . Figures 6a-6b concern an aperture with $\hat{\mathbf{x}} \cos(\pi x/L) \cos(\pi y/L)$ current amplitude pattern, while the line plots of E_{y2} , E_{y3} , and E_{y4} in Figures 6c-6d concern an aperture with $\hat{\mathbf{x}} \cos(\pi x/L) \sin(2\pi y/L)$, $\hat{\mathbf{y}} \cos(\pi x/L) \cos(\pi y/L)$, and $\hat{\mathbf{y}} \sin(2\pi x/L) \cos(\pi y/L)$ surface current distributions (resp.). Note that the polar angle $\theta = 90^\circ$ corresponds to an observation point lying within the central free space layer and thus yields a null scattered-field result. Thus, the polar angle sweep data (both for the first, as well as the latter three, current distribution cases) are shown sub-divided into two plots to remove the artificial discontinuity in the data (versus θ) due to the nature of the scattered-field algorithm. From Figures 6a-6b we see that for $\theta \in [0^\circ, 78^\circ]$ and $\theta \in [102^\circ, 180^\circ]$, one realizes an accuracy between thirteen to fourteen digits in E_x . An analogous statement applies for the error in E_z excepting at $\theta = 0^\circ$ and $\theta = 180^\circ$, where the algorithm's computed solution (to within machine precision) and closed form solution yield answers for E_z having magnitude equal to zero (hence the coercion of the E_z error, at these two angles, to -150dB). We notice that the accuracy degrades as the polar observation angle tends towards horizon, but the algorithm still manages to yield results accurate to approximately three to four digits. Observing the three current cases in Figures 6c-6d leads to similar conclusions for the only non-trivial electric field component E_y : accuracy for E_{y2} and E_{y3} is between thirteen to fourteen digits in the polar range $\theta \in [0^\circ, 78^\circ]$ and $\theta \in [102^\circ, 180^\circ]$, accuracy for E_{y4} is between thirteen to fourteen digits in the polar range $\theta \in [0^\circ, 80^\circ]$ and $\theta \in [100^\circ, 180^\circ]$, all three accuracies degrade for observation points near to the horizon, and for E_{y2} and E_{y4} the accuracy results

at $\theta = 0^\circ$ and $\theta = 180^\circ$ are coerced to -150dB since the computed results (to within machine precision) and validation results were of zero magnitude.

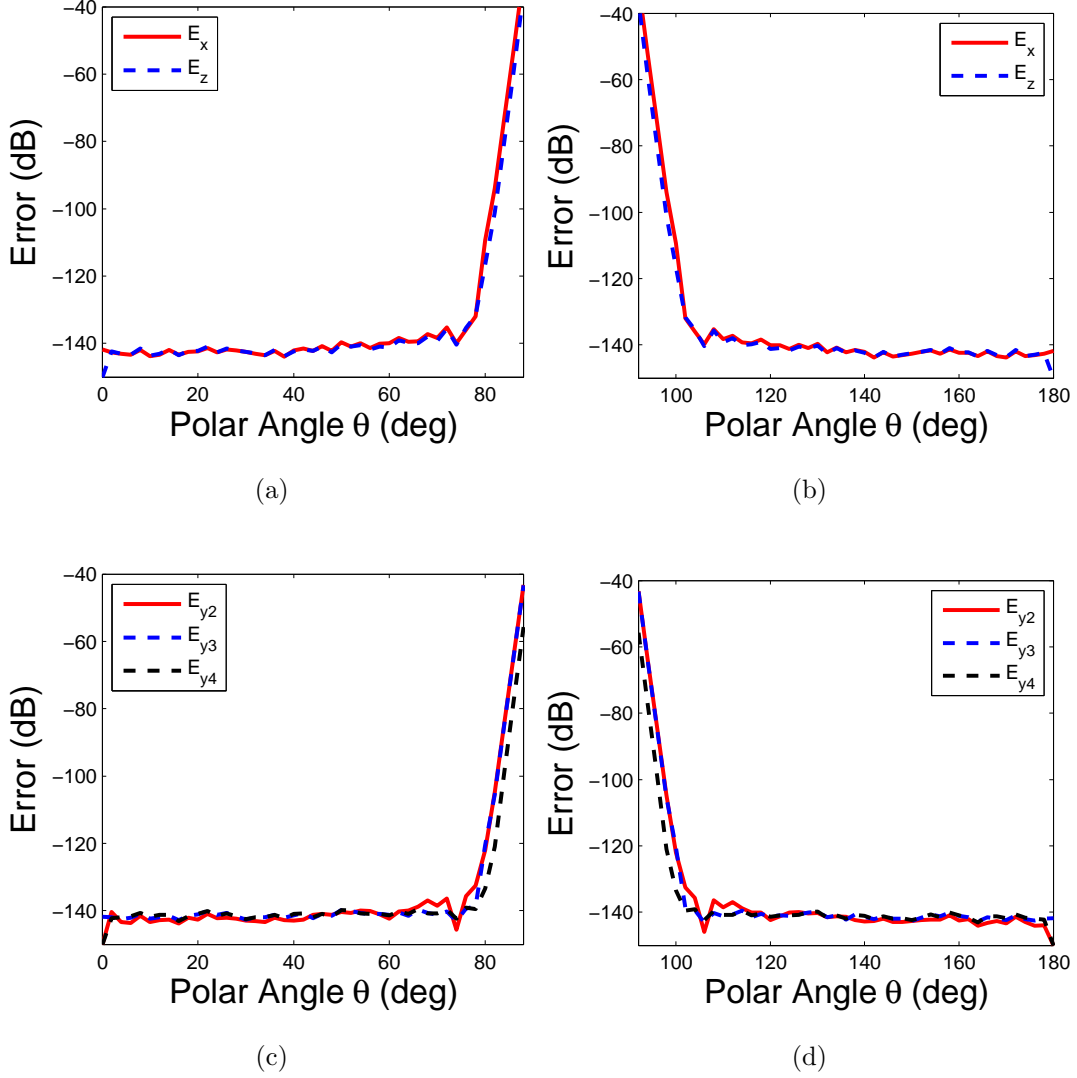


FIG. 6: $\epsilon(\mathcal{E})$ versus θ for the aperture antenna.

Now we show results concerning the algorithm's accuracy computing the magnetic field \mathcal{H} radiated by obliquely-oriented aperture antennas carrying a current distribution $\hat{\mathbf{x}} \cos(\pi \dot{x}/L) \cos(\pi \dot{y}/L)$, which is summarized in Table II. We see that agreement between the algorithm's results and closed-form solutions is again excellent, with at least thirteen digits of accuracy being achieved across both antenna rotation cases. More extensive error studies were performed to better characterize the algorithm's performance, which consisted of all the following parameter permutations: $(E_{\dot{x}}, E_{\dot{y}}, E_{\dot{z}}, H_{\dot{y}}, H_{\dot{z}}) \times (\alpha = 0^\circ, \alpha = 45^\circ, \alpha = 90^\circ) \times (\theta =$

$45^\circ, \theta = 135^\circ) \times (\phi = 0^\circ, \phi = 45^\circ, \phi = 90^\circ, \phi = 135^\circ, \phi = 180^\circ, \phi = 225^\circ, \phi = 270^\circ, \phi = 315^\circ)$. The error results in all these permutations are similar to that shown in Table II. Again, the dot over the field component directions denotes components expressed w.r.t. the antenna's local (rotated) coordinate system.

TABLE II: Relative Error of Magnetic Field $\epsilon(\mathcal{H})$: $\theta = 45^\circ$

α (deg)	ϕ (deg)	$\epsilon(H_{\dot{y}})$ (dB)	$\epsilon(H_{\dot{z}})$ (dB)
45	0	-141	-150
45	45	-142	-142
45	90	-143	-143
45	135	-145	-145
45	180	-140	-150
45	225	-142	-142
45	270	-141	-141
45	315	-145	-145
90	0	-142	-150
90	45	-142	-142
90	90	-144	-144
90	135	-143	-143
90	180	-141	-150
90	225	-142	-142
90	270	-142	-142
90	315	-143	-143

Relative error of \mathcal{H} versus α and ϕ . Adaptive error goal was set to 1.2×10^{-4} .

When comparing the computational time required to obtain the solution (for same accuracy) using the present spectral-domain approach against a conventional (space-domain integration) approach for such aperture radiation scenarios, we found that our numerical experiments demonstrated a factor or approximately two order of magnitudes in solution speed acceleration¹⁷. The reasons for this acceleration factor are the same as those stated

¹⁷ Akin to (and for the same reason as) the analogous wire antenna study, for the space domain approach we do not include the time required to perform the evaluation of the radiation integral (IV.1).

before for the linear antenna case, with the difference being that the relative acceleration factor is now squared (versus the wire antenna case) because of the two-dimensional nature of the spatial domain integration concerning aperture currents.

V. CASE STUDY: MARINE HYDROCARBON EXPLORATION

Next, we illustrate the application of the proposed algorithm for the computation of the scattered-field excited by a wire antenna transmitter operating in a highly inhomogeneous and absorptive marine environment characterizing typical CSEM operational scenarios. CSEM wire antenna transmitters, typically radiating in the frequency range 0.01Hz-10Hz [21], serve as active illuminators to facilitate detection and characterization of thin, highly resistive hydrocarbon-bearing formations embedded deep under the ocean, which are known to be largely invisible to magnetotelluric (MT) sounding-based methods [28]. Indeed, use of an active source allows one to also exploit galvanic, in addition to inductive, generation of the scattered field that arises from blockage, due to a highly resistive layer (e.g., of hydrocarbons), of what was (with the resistive layer absent) a dominantly normally-directed vector current field [31]. Figure 7 below describes the geometry of the problem considered; note that a hydrocarbon-bearing formation buried at 1km under the sea and having 100m thickness is a typical case study found in the related literature [23, 25, 28]. Furthermore, we position the 100m long wire antenna, which is oriented along the positive x direction, such that it resides 50m above the ocean-sediment interface while maintaining the depth of the observation points at the seafloor¹⁸. Furthermore, both the transmitter antenna and observation points are confined to the xz plane. We also remark that since the field strength can vary significantly over the transmitter-receiver separation distances considered herein (1-20km) [28], we plot the magnitude and phase of the *ratio* of the scattered fields received in the two geometries considered in Figures 7a and 7b (see caption of Figure 7 for details of the simulation environment): For example, in the case of E_x^s , we observe the phase and magnitude of the received scattered field ratio $E_{xr}^s = E_{x1}^s/E_{x2}^s$, where E_{x1}^s and E_{x2}^s are the scattered fields observed at a particular receiver in the geometries described by Figures 7a and 7b (resp.). As a result, a measurement's responsiveness to the hydrocarbon formation's

¹⁸ The length, orientation, and depth above the seafloor of the transmitter antenna, as well as the receiver positions, lead to a case study qualitatively following, and is primarily inspired from, the CSEM field campaign reported in [29].

presence is indicated by the extent of phase deviation from 0° (in the phase plot) and the extent of magnitude swing from 0dB (in the magnitude plot).

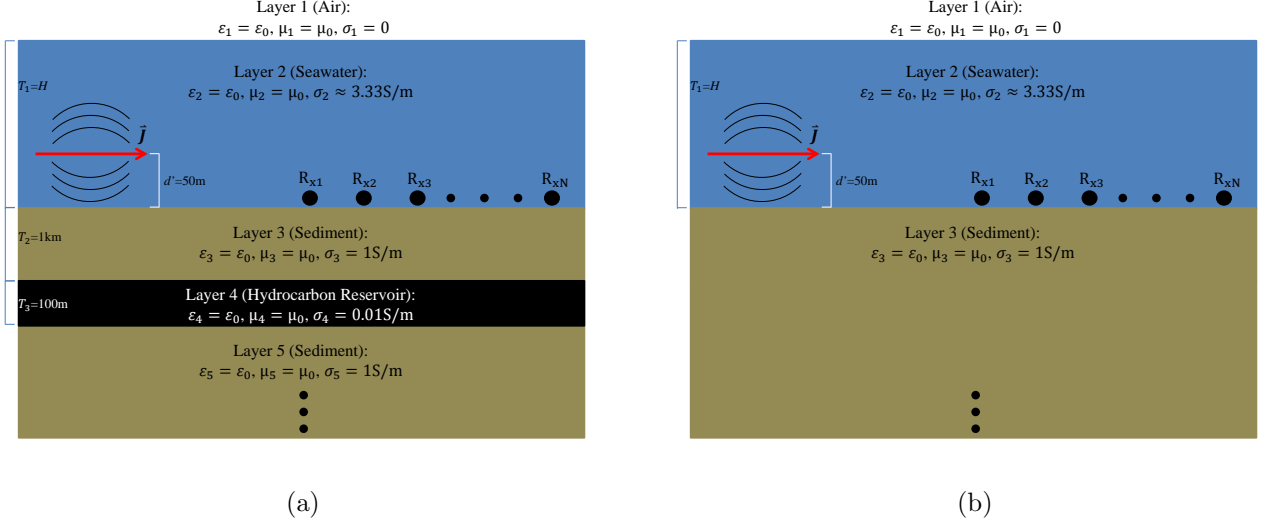


FIG. 7: Schematic illustration of the environment geometries. Figure 7a mirrors Figure 7b except for having a 100m thick, highly resistive hydrocarbon-bearing formation buried 1km beneath the seafloor. The wire antenna's center is positioned at $x=0$, $d' = 50\text{m}$ represents the transmitter height above the seafloor, and the observation points are located at the seafloor.

Figures 8, 9, and 10 illustrate the phase and magnitude of the scattered field ratios concerning E_x^s , H_x^s , and E_z^s (resp.), both for the shallow water ($H=100\text{m}$) and deep water ($H=500\text{m}$) cases¹⁹. From these Figures, we notice that for both seawater depth scenarios the electric field ratios E_x^s and E_z^s (but particularly E_z^s , which corresponds to a pure Transverse-Magnetic to z mode [TM_z] [38, 57]) exhibit strong responsiveness to the presence of the deeply buried hydrocarbon bed. On the other hand, in shallow water H_x^s provides little useful information, as can be seen by its relatively poor response to the presence of the resistive hydrocarbon formation compared to the electric field measurements. However, upon increasing the water depth to 500m, both the phase and magnitude of H_{xr}^s show a very high response to the presence of the hydrocarbon bed. Unfortunately, the phase and magnitude of H_{zr}^s (not shown here), corresponding to a pure Transverse-Electric to z mode

¹⁹ In the top-left corner of Figure 9c, note the vortex-like behavior of the phase. The seemingly solid vertical black strip corresponds to closely spaced (black) contour lines that, upon zooming in at high resolution, do in fact illustrate the locally rapid variation of phase.

(TE_z) [38, 57], fails to yield significant responsiveness to the resistive formation even when the water depth is increased to 500m. All these results corroborate prior studies indicating that the sea-air interface can support a strong, slowly decaying “air-wave” masking the hydrocarbon formation’s effect on the electric and magnetic field measurements [22, 24, 25]. However, the masking effect is strongly dependent on the field type and component, with the masking effect much more pronounced in measurements derived from the TE_z modes compared to the TM_z modes [22, 24, 25].

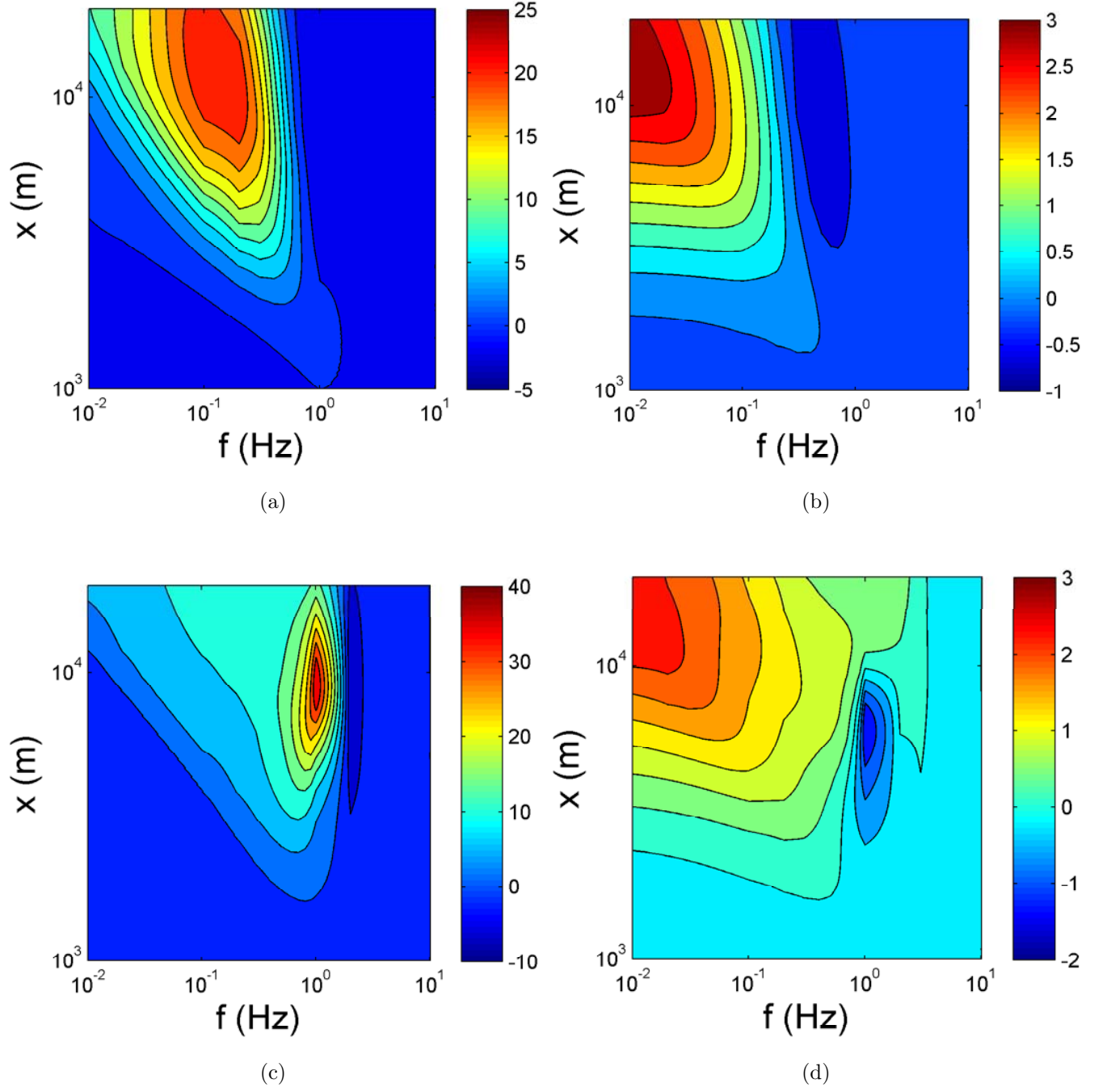


FIG. 8: Figures 8a and 8c denote the phase (degrees) of E^s_{xr} when the transmitter operates (resp.) in either shallow water ($H=100$ m) or deep water ($H=500$ m), while Figures 8b and 8d denote the magnitude (dB) of E^s_{xr} when the transmitter operates (resp.) in either shallow water ($H=100$ m) or deep water ($H=500$ m).

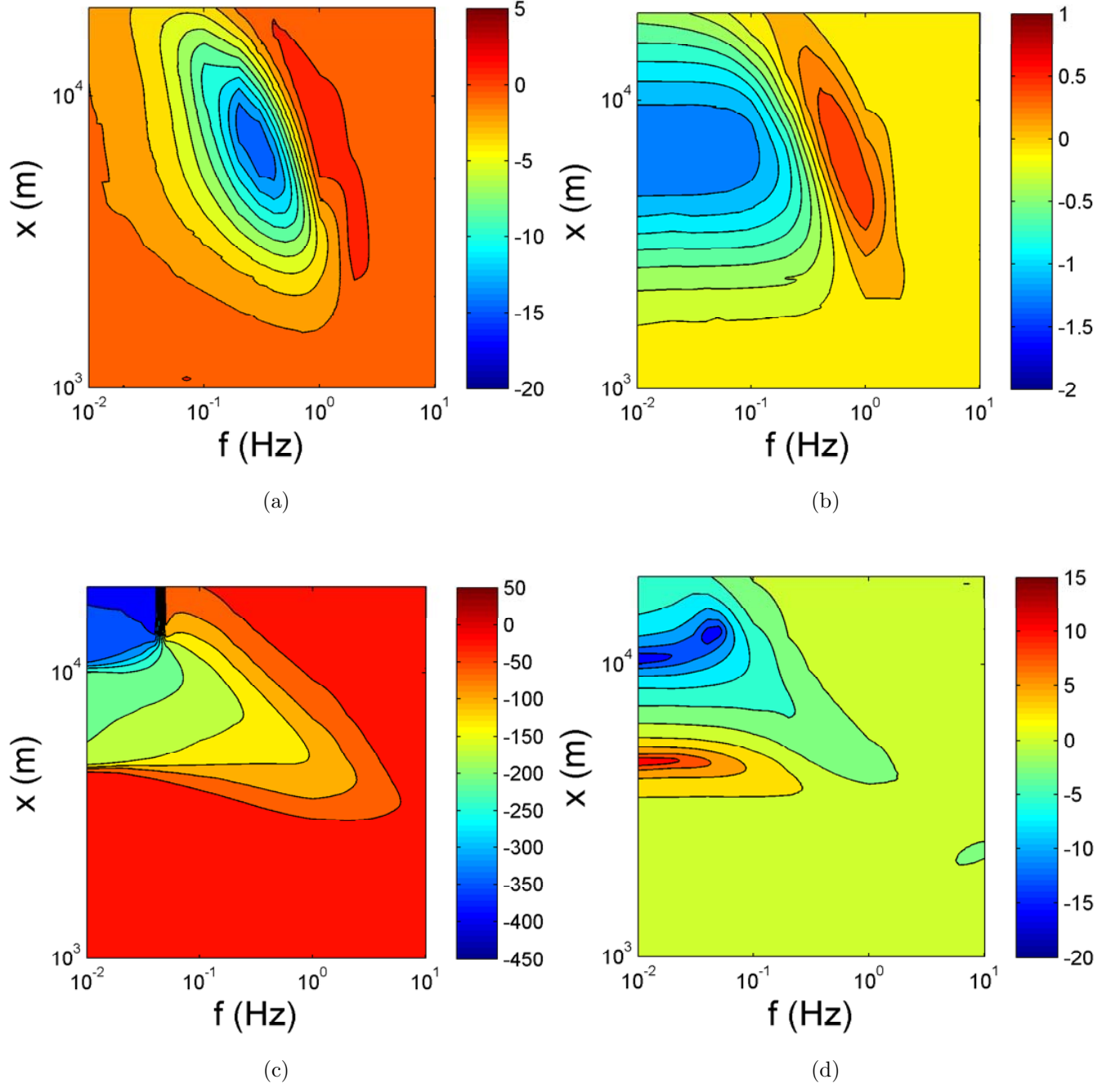


FIG. 9: Figures 9a and 9c denote the phase (degrees) of H^s_{xr} when the transmitter operates (resp.) in either shallow water ($H=100$ m) or deep water ($H=500$ m), while Figures 9b and 9d denote the magnitude (dB) of H^s_{xr} when the transmitter operates (resp.) in either shallow water ($H=100$ m) or deep water ($H=500$ m).

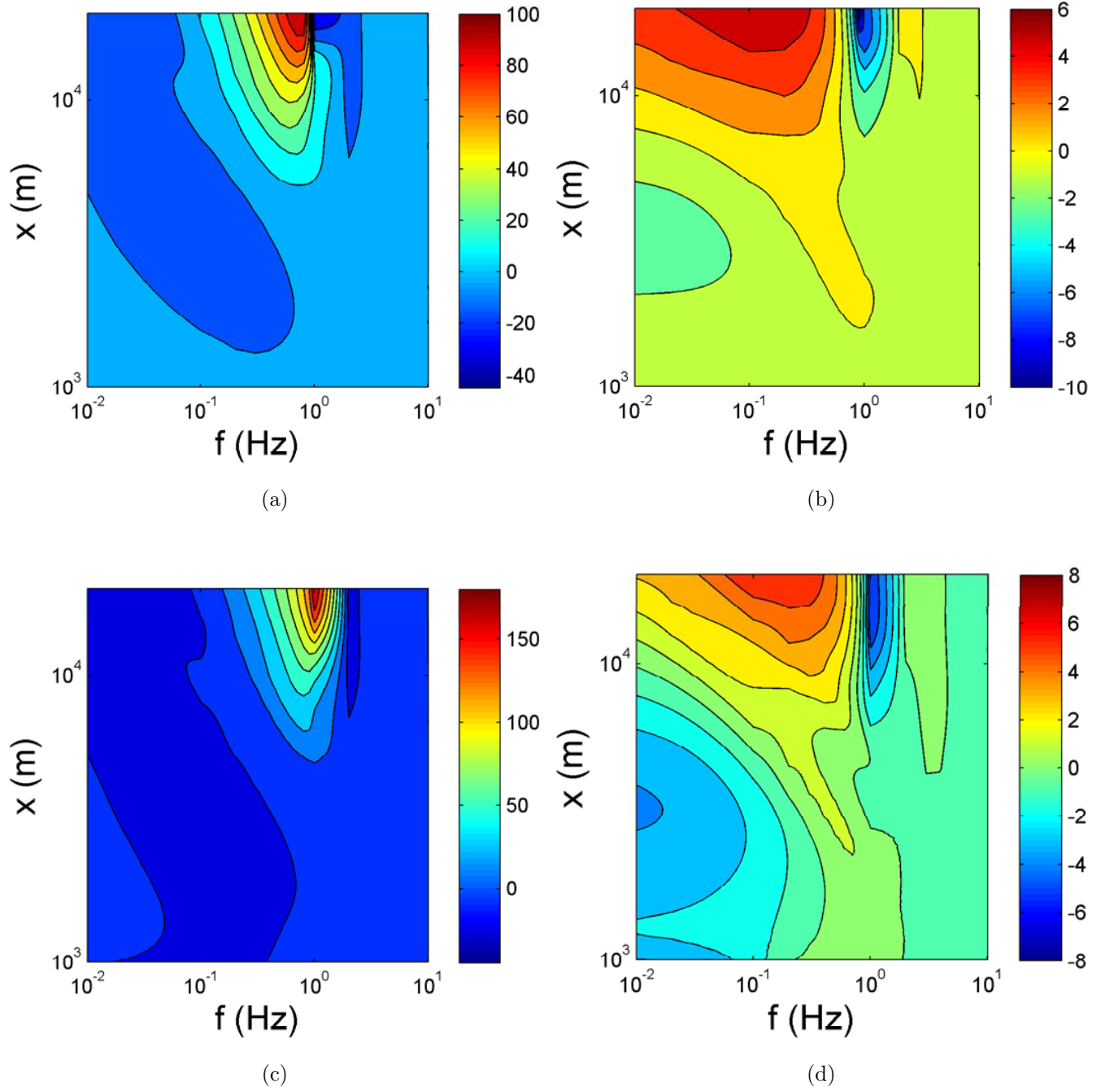


FIG. 10: Figures 10a and 10c denote the phase (degrees) of E_{zr}^s when the transmitter operates (resp.) in either shallow water ($H=100$ m) or deep water ($H=500$ m), while Figures 10b and 10d denote the magnitude (dB) of E_{zr}^s when the transmitter operates (resp.) in either shallow water ($H=100$ m) or deep water ($H=500$ m).

VI. CONCLUDING REMARKS

We have introduced and validated a numerical algorithm to extract the scattered field manifesting within planar-stratified environments with embedded distributed sources (e.g., aperture or linear antennas) based on spectral-domain integrals. Some of the key features of the proposed algorithm are: (1) Numerical robustness under large variations on the problem parameters and source-observation separations, (2) non-reliance on space domain tensor Green’s functions and hence applicability to arbitrarily anisotropic media (layers), (3) no added computational burden versus a prior state-of-the-art algorithm used to compute the total field from point sources [32] (instead, further acceleration is achieved by the extra integrand decay provided by the source spectrum’s multiplicative tapering effect), and (4) applicability to any distributed source admitting a modal field synthesis. To validate the algorithms, numerical results were compared against closed-form field solutions when the latter are available. To further illustrate the applicability of the algorithm, we applied it to the modeling of CSEM method sensing of sub-oceanic hydrocarbon deposits using active wire antenna transmitters.

VII. ACKNOWLEDGMENTS

This work was primarily supported by a NASA Space Technology Research Fellowship (NSTRF). We also acknowledge partial support from the Ohio Supercomputer Center under Grants PAS-0061 and PAS-0110. We thank Dr. Burkay Donderici of Halliburton Energy Services for initial impetus for this research. KS acknowledges Dr. Anthony Freeman of the NASA/JPL for his mentorship under the NSTRF program.

VIII. REFERENCES

-
- [1] S. Davydycheva and T. Wang, in *SEG Annual Meeting* (2011) pp. 494–498.
 - [2] B. Wei, T. Wang, and Y. Wang, *Chinese Journal of Geophysics* **52**, 1350 (2009).

- [3] B. I. Anderson, T. D. Barber, and S. C. Gianzero, in *SPWLA 39th Annual Logging Symposium* (1998) pp. 1–14.
- [4] B. I. Anderson, S. Bonner, M. G. Luling, and R. Rosthal, in *SPWLA 31st Annual Logging Symposium* (1990) pp. 1–25, paper A.
- [5] A. Howard Jr., *IEEE Transactions on Antennas and Propagation* **48**, 1376 (2000).
- [6] M. Zhdanov, W. Kennedy, and E. Peksen, *Petrophysics* **42**, 588 (2001).
- [7] H. Wang, H. Tao, J. Yao, G. Chen, and S. Yang, *Chinese Journal of Geophysics* **51**, 1110 (2008).
- [8] J. Moran and S. Gianzero, *Geophysics* **44**, 1266 (1979), <http://library.seg.org/doi/pdf/10.1190/1.1441006>.
- [9] D. Georgi, J. Schoen, and M. Rabinovich, in *SPE Annual Technical Conference and Exhibition* (2008) pp. 1–18.
- [10] S. Liu and M. Sato, in *SPWLA 43rd Annual Logging Symposium* (2002) pp. 1–14.
- [11] L. Chen, *The Log Analyst* **30**, 217 (1989).
- [12] H. O. Lee and F. L. Teixeira, *IEEE Transactions on Geoscience and Remote Sensing* **45**, 383 (2007).
- [13] H. O. Lee, F. L. Teixeira, L. E. S. Martin, , and M. S. Bittar, *IEEE Transactions on Geoscience and Remote Sensing* **50**, 727 (2012).
- [14] H. Odabasi and F. Teixeira, *Radio Science* **47**, 1 (2012).
- [15] D. Pozar and V. Sanchez, *Electronics Letters* **24**, 729 (1988).
- [16] D. M. Pozar, *IEEE Transactions on Antennas and Propagation* **35**, 613 (1987).
- [17] A. Polycarpou and C. Balanis, in *IEEE Antennas and Propagation Society International Symposium 1999*, Vol. 1 (1999) pp. 666–669 vol.1.
- [18] M. Paulus, P. Gay-Balmaz, and O. J. F. Martin, *Phys. Rev. E* **62**, 5797 (2000).
- [19] M. Jehle, M. Ruegg, L. Zuberbuhler, D. Small, and E. Meier, *IEEE Transactions on Geoscience and Remote Sensing* **47**, 1512 (2009).
- [20] G. Gentili and U. Spagnolini, *IEEE Transactions on Geoscience and Remote Sensing* **38**, 1936 (2000).
- [21] David Andreis and Lucy MacGregor, *Geophysics* **73**, F21 (2008).
- [22] D. Andreis and L. MacGregor, “TimeDomain Versus FrequencyDomain CSEM in Shallow Water,” in *SEG Technical Program Expanded Abstracts 2007*, Chap. 130, pp. 643–647,

- <http://library.seg.org/doi/pdf/10.1190/1.2792500>.
- [23] Kerry Key, *Geophysics* **74**, F9 (2009).
 - [24] Dylan Connell and Kerry Key, *Geophysical Prospecting* **61**, 187 (2013).
 - [25] Chester Weiss, *Geophysics* **72**, A93 (2007).
 - [26] Peter Weidelt, *Geophysical Journal International* **171**, 153 (2007).
 - [27] Steven Constable and Leonard J. Srnka, *Geophysics* **72**, WA3 (2007).
 - [28] Steven Constable and Chester Weiss, *Geophysics* **71**, G43 (2006).
 - [29] S. Ellingsrud, T. Eidesmo, S. Johansen, M. Sinha, L. MacGregor, and S. Constable, *Leading Edge* **21**, 972 (2002).
 - [30] T. Eidsmo, S. Ellingsrud, L. MacGregor, S. Constable, M. Sinha, S. Johansen, F. Kong, , and H. Westerdahl, *First Break* **20**, 144 (2002).
 - [31] E. Um and D. Alumbaugh, *Geophysics* **72**, WA13 (2007).
 - [32] K. Sainath, F. L. Teixeira, and B. Donderici, *Phys. Rev. E* **89**, 013312 (2014).
 - [33] K. Sainath, F. L. Teixeira, and B. Donderici, (2013), available: <http://arxiv.org/abs/1311.0582v1> (To Appear 2014).
 - [34] K. Sainath and F. L. Teixeira, *Phys. Rev. E* (2014), under Review.
 - [35] K. A. Michalski, in *Workshop on Integral Techniques for Electromagnetics* (Lausanne, Switzerland, 2007) pp. 1–47.
 - [36] J. Mosig, *IEEE Transactions on Antennas and Propagation* **60**, 2011 (2012).
 - [37] K. A. Michalski, *IEEE Transactions on Antennas and Propagation* **46**, 1405 (1998).
 - [38] W. C. Chew, *Waves and Fields in Inhomogeneous Media* (Van Nostrand Reinhold, 1990).
 - [39] A. Alparslan, M. Aksun, and K. Michalski, *IEEE Transactions on Microwave Theory and Techniques* **58**, 602 (2010).
 - [40] A. Caboussat and G. Miers, *Computers & Mathematics with Applications* **59**, 338 (2010).
 - [41] T. Matsuoka and M. Tateiba, in *IEEE Antennas and Propagation Society International Symposium, 2003*, Vol. 1 (2003) pp. 561–564 vol.1.
 - [42] A. Tabatabaeenejad and M. Moghaddam, *Geoscience and Remote Sensing, IEEE Transactions on* **44**, 2102 (2006).
 - [43] A. Fiori, A. Benedetto, and M. Romanelli, *Geophysical Research Letters* **32**, 1 (2005).
 - [44] X. Zhan, P. Houser, J. Walker, and W. Crow, *IEEE Transactions on Geoscience and Remote Sensing* **44**, 1534 (2006).

- [45] S. V. Nghiem, R. Kwok, J. A. Kong, and R. T. Shin, *Radio Science* **28**, 687 (1993).
- [46] Y. Lasne, P. Paillou, A. Freeman, T. Farr, K. McDonald, G. Ruffie, J. Malezieux, B. Chapman, and F. Demontoux, *IEEE Transactions on Geoscience and Remote Sensing* **46**, 1674 (2008).
- [47] A. Sommerfeld, *Annalen der Physik* **333**, 665 (1909).
- [48] S. Lambot, E. Slob, and H. Vereecken, *Geophysical Research Letters* **34**, 1 (2007).
- [49] J. Liu, Y. Kuga, A. Ishimaru, X. Pi, and A. Freeman, *IEEE Transactions on Geoscience and Remote Sensing* **41**, 939 (2003).
- [50] X. Pi, A. Freeman, B. Chapman, P. Rosen, and Z. Li, *Journal of Geophysical Research: Space Physics* **116**, n/a (2011).
- [51] C. A. Balanis, *Antenna Theory: Analysis and Design* (Wiley-Interscience, 2005).
- [52] K. T. R. Davies, *Journal of Physics G: Nuclear Physics* **14**, 973 (1988).
- [53] W. Barclay and P. Marinos, in *IRE International Convention Record*, Vol. 13 (1965) pp. 155–158.
- [54] R. Jorgensen, *IEE Proceedings H: Microwaves, Optics and Antennas* **127**, 201 (1980).
- [55] G. Stewart, *Linear Algebra and its Applications* **283**, 151 (1998).
- [56] P. Clemmow, “The plane wave spectrum representation of electromagnetic fields,” (IEEE Press, Piscataway, NJ, 1996).
- [57] L. B. Felsen and N. Marcuvitz, “Radiation and Scattering of Waves,” (IEEE Press, Piscataway, NJ, 1994) Chap. 7, pp. 740–820.